Molecular Cell

Article

Stress Induces Dynamic, Cytotoxicity-Antagonizing TDP-43 Nuclear Bodies via Paraspeckle LncRNA *NEAT1*-Mediated Liquid-Liquid Phase Separation

Graphical Abstract

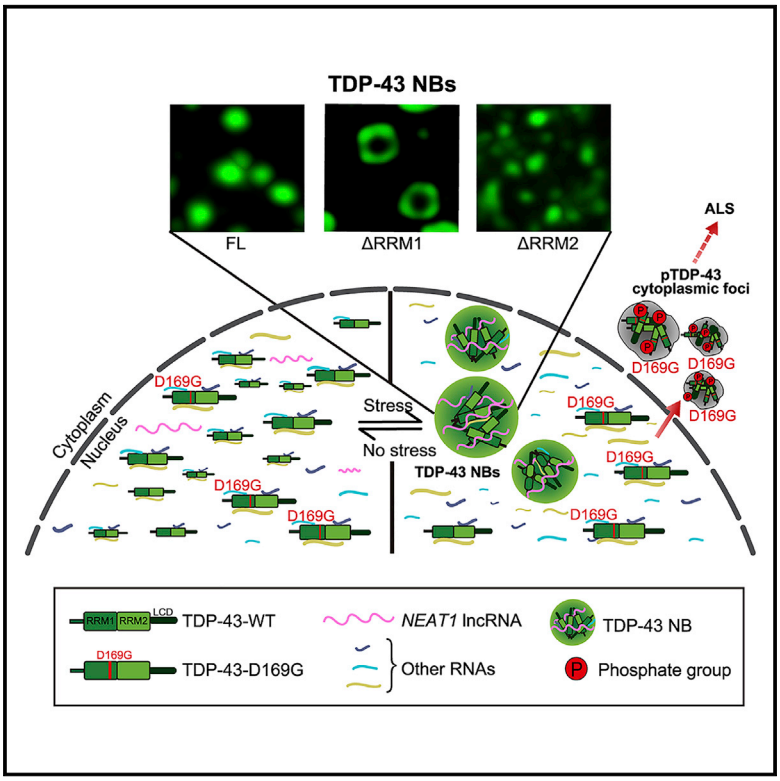

Highlights

- Stress induces phase-separated TDP-43 NBs to alleviate cytotoxicity
- The two RRMs respond to different RNAs and act distinctly in the assembly of TDP-43 NBs
- LncRNA *NEAT1* promotes TDP-43 LLPS and is upregulated in stressed neurons
- The ALS-causing D169G mutation is NB-defective and forms pTDP-43 cytoplasmic foci

Authors

Chen Wang, Yongjia Duan, Gang Duan, ..., Lin Guo, Cong Liu, Yanshan Fang

Correspondence

liulab@sioc.ac.cn (C.L.), fangys@sioc.ac.cn (Y.F.)

In Brief

The RNA-binding protein TDP-43 is associated with neurodegenerative diseases, such as ALS. Wang et al. report that TDP-43 forms protective nuclear bodies in response to stress, which is mediated by lncRNA *NEAT1*-promoted liquid-liquid phase separation. Defects in the assembly of stress-mitigating TDP-43 nuclear bodies may contribute to ALS pathogenesis.

Wang et al., 2020, Molecular Cell *79*, 443–458
August 6, 2020
https://doi.org/10.1016/j.molcel.2020.06.019

CellPress

Molecular Cell

CellPress

Article

Stress Induces Dynamic, Cytotoxicity-Antagonizing TDP-43 Nuclear Bodies via Paraspeckle LncRNA *NEAT1*-Mediated Liquid-Liquid Phase Separation

Chen Wang,[1,2,4] Yongjia Duan,[1,2,4] Gang Duan,[1,2,4] Qiangqiang Wang,[1] Kai Zhang,[1,2] Xue Deng,[1,2] Beituo Qian,[1,2] Jinge Gu,[1,2] Zhiwei Ma,[1,5] Shuang Zhang,[1] Lin Guo,[3] Cong Liu,[1,2,*] and Yanshan Fang[1,2,6,*]

[1]Interdisciplinary Research Center on Biology and Chemistry, Shanghai Institute of Organic Chemistry, Chinese Academy of Sciences, Shanghai 201210, China

[2]University of Chinese Academy of Sciences, Beijing 100049, China

[3]Department of Biochemistry and Molecular Biology, Thomas Jefferson University, Philadelphia, PA 19107, USA

[4]These authors contributed equally

[5]Present address: West China School of Basic Medical Sciences and Forensic Medicine, Sichuan University, Chengdu 610041, China

[6]Lead Contact

*Correspondence: liulab@sioc.ac.cn (C.L.), fangys@sioc.ac.cn (Y.F.)

https://doi.org/10.1016/j.molcel.2020.06.019

SUMMARY

Despite the prominent role of TDP-43 in neurodegeneration, its physiological and pathological functions are not fully understood. Here, we report an unexpected role of TDP-43 in the formation of dynamic, reversible, liquid droplet-like nuclear bodies (NBs) in response to stress. Formation of NBs alleviates TDP-43-mediated cytotoxicity in mammalian cells and fly neurons. Super-resolution microscopy reveals distinct functions of the two RRMs in TDP-43 NB formation. TDP-43 NBs are partially colocalized with nuclear paraspeckles, whose scaffolding lncRNA *NEAT1* is dramatically upregulated in stressed neurons. Moreover, increase of *NEAT1* promotes TDP-43 liquid-liquid phase separation (LLPS) *in vitro*. Finally, we discover that the ALS-associated mutation D169G impairs the *NEAT1*-mediated TDP-43 LLPS and NB assembly, causing excessive cytoplasmic translocation of TDP-43 to form stress granules, which become phosphorylated TDP-43 cytoplasmic foci upon prolonged stress. Together, our findings suggest a stress-mitigating role and mechanism of TDP-43 NBs, whose dysfunction may be involved in ALS pathogenesis.

INTRODUCTION

Amyotrophic lateral sclerosis (ALS) is a neurological disorder characterized by degeneration of motor neurons in the brain and spinal cord (Taylor et al., 2016; van Es et al., 2017). Missense mutations in the gene *TARDBP* encoding TAR DNA-binding protein 43 (TDP-43) predispose to familial ALS, and protein inclusions containing TDP-43 are a pathological hallmark of ALS (Neumann et al., 2006; Kabashi et al., 2008). TDP-43 has a nuclear localization signal (NLS), a nuclear export signal (NES), two canonical RNA recognition motifs (RRMs), and a C-terminal low complexity domain (LCD). The LCD mediates protein-protein interactions and is enriched with disease-associated mutations (Kabashi et al., 2008; Lee et al., 2011). TDP-43 is engaged in a variety of ribonucleoprotein (RNP) complexes, such as stress granules (SGs), and regulates RNA processing and homeostasis (Fahrenkrog and Harel, 2018; Zhao et al., 2018). In diseased conditions, SGs may undergo aberrant phase transition and promote the formation of solid protein aggregates (Li et al., 2013; Ramaswami et al., 2013).

Nuclear bodies (NBs) are dynamic, membraneless nuclear structures that concentrate specific nuclear proteins and RNAs to regulate nuclear functions and homeostasis (Staněk and Fox, 2017). Among them, paraspeckles (PSs) are a class of nuclear RNP granules formed by the scaffolding long non-coding RNA (lncRNA) nuclear-enriched abundant transcript 1 (*NEAT1*), associated with proteins such as splicing factor proline-glutamine rich (SFPQ) and P54NRB/NONO. PSs are engaged in regulating cellular functions through nuclear retention of mRNAs and proteins (Bond and Fox, 2009; Fox and Lamond, 2010; Nakagawa et al., 2018). Notably, TDP-43 is found colocalized with PSs in the spinal motor neurons of ALS patients (Nishimoto et al., 2013), and excessive PSs are also observed in ALS-FUS patients (An et al., 2019a). Although TDP-43 is present in NBs that sometimes accompany neurodegeneration, the understanding about the function of TDP-43 in NBs and the involvement of NBs in ALS pathogenesis is still rudimentary.

Recent studies indicate that liquid-liquid phase separation (LLPS) of RNA-binding protein (RBP) drives the assembly of liquid droplet (LD)-like, membraneless RNP granules in cells (Lin et al., 2015; Feric et al., 2016; Banani et al., 2017; Uversky, 2017; Fox et al., 2018). Several ALS-related RBPs, including TDP-43, are shown to phase separate *in vitro* (Hyman et al.,

2014; Molliex et al., 2015; Schmidt and Rohatgi, 2016), and the intrinsically disordered LCD domains of the RBPs are thought to mediate the LLPS (Hennig et al., 2015; Molliex et al., 2015; Xiang et al., 2015; Murray et al., 2017). RNA is also of vital importance in regulating the LLPS (Dominguez et al., 2018; Namkoong et al., 2018; Fox et al., 2018), which can suppress or promote phase separation depending on the contents and concentrations of the RNAs (Shevtsov and Dundr, 2011; Lin et al., 2015; Maharana et al., 2018; Mann et al., 2019).

In this study, we find that stress causes TDP-43 to form dynamic, reversible, and cytotoxicity-antagonizing NBs. Further investigations reveal distinct functions of the two RRMs and a crucial role of *NEAT1* lncRNA in regulating TDP-43 LLPS and NB formation, which is compromised by the ALS-causing mutation D169G, leading to hyperphosphorylated TDP-43 cytoplasmic foci and reduced tolerance to stress. Together, we propose that stress induces LLPS and the assembly of TDP-43 NBs in the generally suppressive nucleoplasm via upregulation of lncRNA *NEAT1*, and defective stress-mitigating TDP-43 NBs may contribute to ALS pathogenesis.

RESULTS

Arsenic Stress Induces Dynamic and Reversible TDP-43 NBs

TDP-43 is predominantly in the nucleus but recruited to cytoplasmic SGs in response to stress (Li et al., 2013). Interestingly, in an earlier related work (Duan et al., 2019), we noticed that although arsenic stress induced TDP-43^{+} cytoplasmic SGs, the majority of TDP-43-HA signals remained nuclear. In these cells, nuclear TDP-43 lost the normal diffused pattern but displayed a distinct granular appearance (Figures 1A and 1B; Video S1). Endogenous TDP-43 also formed nuclear granules upon stress (Figures 1C–1E), indicating that this phenomenon was not an artificial effect simply due to TDP-43 overexpression (OE).

A membraneless nuclear structure fulfills the requirements of NBs if it is (1) microscopically visible, (2) enriched with specific nuclear factors, and (3) continuously exchanging with the surrounding nucleoplasm (Staněk and Fox, 2017). Arsenite-induced TDP-43 nuclear granules were microscopically visible (Figures 1A–1E) and partially colocalized with several types of NBs, especially PSs labeled by SFPQ (Figure S1).

To examine whether the stress-induced TDP-43 nuclear granules were dynamic, we performed the fluorescence recovery after photobleaching (FRAP) analysis in *live* cells using green fluorescent protein (GFP)-tagged TDP-43. The fluorescence of GFP-TDP-43 nuclear granules was rapidly recovered after photobleaching, reaching ~50% of the pre-bleaching intensity in ~65 s (Figures 1F–1H; Video S2), indicating that these nuclear granules are LD-like and highly dynamic. As they fulfilled the three requirements of NBs, we named them "TDP-43 NBs" thereafter in this study.

Next, we determined whether stress-induced TDP-43 NBs were reversible. Cells were treated with arsenite for 30 min to induce the formation of TDP-43 NBs. Of note, some of the NBs were not perfectly round (Figure 1I), which might be a sign of the start of phase transition toward the less dynamic aggregates as shown in Figure 1G with prolonged stress (6 h). With prompt arsenite washout, TDP-43 NBs gradually disappeared and eventually recovered to nearly diffused pattern (Figure 1I). Both the percentages of cells showing TDP-43 NBs and the counts of TDP-43 NBs per cell decreased in a time-dependent manner after arsenite washout (Figures 1J–1L). Thus, arsenite-induced TDP-43 NBs are reversible.

Formation of TDP-43 NBs Acts as a General Cellular Stress Mechanism

Reversible TDP-43 nuclear aggregation was previously observed with heat shock (Udan-Johns et al., 2014). To determine whether other types of stress could induce TDP-43 NBs, we disturbed the nuclear homeostasis by inhibition of nuclear export with leptomycin B (LMB), which caused endogenous TDP-43 to form NBs (Figures 2A and 2B), suggesting that the assembly of TDP-43 NBs might be a general mechanism employed by the nucleus in response to stress.

Next, we sought to test whether blocking the nuclear export of TDP-43 itself was sufficient to induce TDP-43 NBs. A few recent works indicated that the NES sequence lacked functional export activity (Archbold et al., 2018; Ederle et al., 2018; Pinarbasi et al., 2018); nevertheless, nuclear TDP-43 puncta with resemblance to NBs upon deletion of this domain were evident as previously reported (Ayala et al., 2008; Winton et al., 2008). Thus, we generated the so-called NLS^{mut} and NES^{mut} TDP-43 (Figure 2C). TDP-43-NLS^{mut} was predominantly cytoplasmic with no or few NBs; in contrast, the NES^{mut} was exclusively nuclear and formed striking NBs in the absence of stress (Figures 2D–2F). The solubility of TDP-43-NES^{mut} protein was significantly reduced (Figures 2G and 2H). Of note, the total protein levels of NLS^{mut} and NES^{mut} are not statistically different from that of wild-type (WT) TDP-43 ($p = 0.8451$ and 0.2835, respectively).

The marked reduction of the solubility raised the question whether TDP-43-NES^{mut} NBs were still dynamic or were solid aggregates. We then performed the FRAP assay on the NES^{mut} NBs. Similar to the PS protein SFPQ, the fluorescence signal of GFP-TDP-43-NES^{mut} rapidly recovered (Figures S2A and S2B). None of WT, NLS^{mut}, or NES^{mut} TDP-43 in the soluble fractions showed significant turnover in 24 h after the inhibition of cellular protein synthesis with cycloheximide (CHX) (Figures S2C–S2F), suggesting that the soluble TDP-43 protein was rather stable. In contrast, the insoluble fraction of TDP-43-NES^{mut} decreased rapidly upon CHX inhibition (Figures S2C–S2F), and NES^{mut} NBs were disassembled (Figures S2G and S2H), indicating that TDP-43-NES^{mut} NBs were dynamic and reversible.

Next, we examined how disturbance of the proteostasis in cells impacted TDP-43 NBs. Inhibition of proteasome-mediated protein degradation by MG132 led to a significant increase in the insoluble fractions of WT and NES^{mut} TDP-43 protein (Figures S2I–S2L). In contrast, blocking autophagic flux by chloroquine (CQ) did not significantly affect the levels of insoluble TDP-43 (Figures S2M–S2P). Thus, unlike protein aggregates, the turnover of TDP-43 NBs did not rely on the autophagy-lysosomal pathway. Together, TDP-43 NBs are distinct from misfolded protein aggregates. Instead, they are dynamic, reversible subnuclear organelles that are sensitive to changes in the microenvironment of the nucleoplasm.

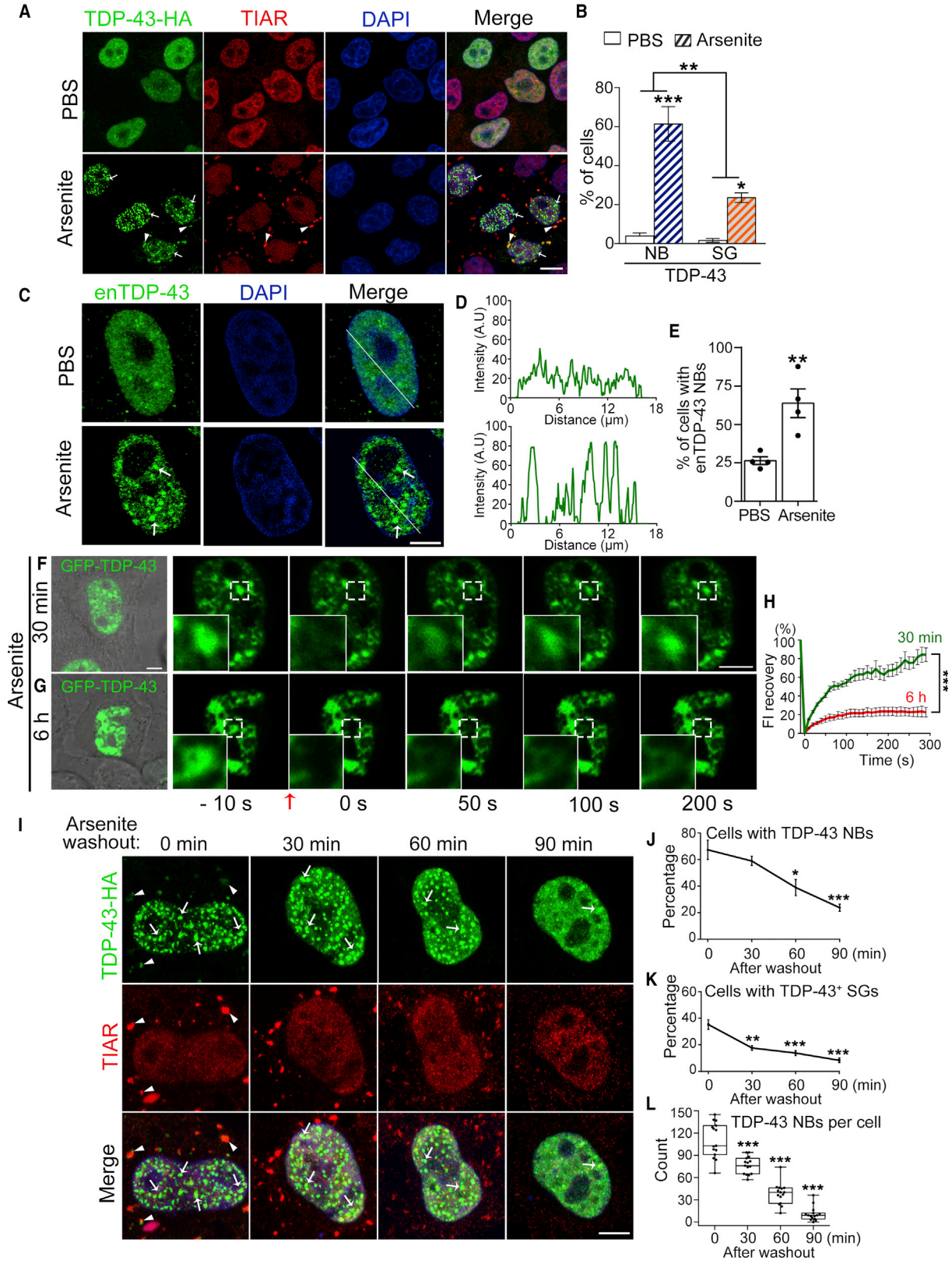

(legend on next page)

Formation of TDP-43 NBs Alleviates the Cytotoxicity in Mammalian Cells and Fly Neurons

To understand the functional significance of forming TDP-43 NBs, we examined how cells expressing WT, NLS^{mut}, or NES^{mut} TDP-43 responded to stress. Compared to WT TDP-43, cells transfected with the NLS^{mut} showed significantly increased cell death assessed by propidium iodide (PI) staining, whereas the NES^{mut} was more resistant to arsenic stress (Figures S3A–S3E′). Next, we examined how the formation of NBs impacted TDP-43 cytotoxicity. We found that in the absence of arsenic stress, OE of WT or NLS^{mut}, but not NES^{mut}, TDP-43 was sufficient to significantly decrease the cell viability (Figure 3A) and the ATP levels (Figure 3B) in human 293T cells. These results were consistent with the previous studies that cytoplasmic TDP-43 was more toxic than nuclear TDP-43 in flies (Miguel et al., 2011) and primary rat neurons (Barmada et al., 2010); however, the reduced cytotoxicity was not associated with the NB formation of nuclear TDP-43 before.

To examine whether TDP-43 form NBs *in vivo* and how they impact neurodegeneration, we generated transgenic flies to express WT, NLS^{mut}, or NES^{mut} human TDP-43 (hTDP-43) by ΦC31-mediated, site-specific integration (Groth et al., 2004; Bateman et al., 2006). WT and NES^{mut} hTDP-43 in fly neurons (*elav*-Gal4) were predominantly nuclear, whereas the NLS^{mut} was mostly cytoplasmic (Figure S4A). Consistent with the mammalian data, NES^{mut} hTDP-43 formed NBs in the nucleus of fly neurons (Figures S4A and S4B), and the solubility was significantly decreased (Figures S4C and S4D). The eye degeneration analysis (Figure S4E) and the climbing assay (Figure S4F) showed that WT TDP-43 flies exhibited marked age-dependent degenerative phenotypes, and the NLS^{mut} flies were significantly worse. In contrast, the NES^{mut} was substantially less toxic, especially in the ALS-related functional assay of the climbing capability (Figure S4F).

To confirm whether it was the formation of TDP-43 NBs that underlay the cytotoxicity-mitigating effect rather than simply the restriction of TDP-43 in the nucleus, we sought for alternative approaches to induce TDP-43 NBs without disrupting their nucleocytoplasmic transport. Acetylation of TDP-43 at K145 and K192 was previously shown to regulate RNA binding and affect TDP-43 aggregation (Cohen et al., 2015). Indeed, the K145/192Q mutation in WT TDP-43 (Figure 3C) led to the assembly of TDP-43 NBs in the absence of stress (Figures 3E, 3E′, and 3G). On the other hand, the K145/192R mutation in TDP-43-NES^{mut} (Figure 3D) abolished the spontaneous formation of NES^{mut} NBs (Figures 3F, 3F′, and 3H). Neither of the mutations significantly altered the subcellular distribution of TDP-43 (Figures 3I and 3J). Supporting our hypothesis, the NB-forming K145/192Q mutation alleviated the cytotoxicity of WT TDP-43 (Figure 3K), whereas the K145/192R mutation abolished the NB-forming capability and made the originally non-toxic TDP-43-NES^{mut} manifest marked cytotoxicity (Figure 3L).

The Role of the Major Functional Domains of TDP-43 in the Assembly of NBs

Next, we generated truncated TDP-43, namely ΔLCD, ΔRRM1, and ΔRRM2, to investigate the role of each major domain in the NB formation (Figure S5A). ΔLCD TDP-43 was mostly nuclear and soluble (Figures S5B and S5C) but did not form NBs in response to stress (Figures S5F–S5G′). TDP-43-ΔRRM1 was soluble (Figure S5D), whereas ΔRRM2 showed a remarkable increase of insolubility (Figure S5E). More interestingly, TDP-43-ΔRRM1 formed large, ring-shaped nuclear structures in the absence of stress (Figures S5H and S5H′). The ΔRRM2 looked similar to WT TDP-43 without stress but showed a grainy appearance when stressed (Figures S5I and S5I′). We further characterized these nuclear structures with the LIGHTNING super-resolution microscopy: WT TDP-43 formed solid, mid-size NBs; ΔRRM1 was much larger and ring-shaped; and ΔRRM2 displayed a mesh-like structure with numerous smaller NBs (Figures 4A and 4B). Three-dimensional (3D) rendering revealed that WT and ΔRRM2 TDP-43 NBs were mostly ovals or sometimes cylinders, whereas ΔRRM1 were large, hollow pillars. Measurement of the diameters further confirmed that ΔRRM1 rings were drastically larger than WT TDP-43 NBs, whereas ΔRRM2 NBs were slightly smaller (Figure 4C).

Given the distinct morphology of the nuclear structures formed by ΔRRM1 and ΔRRM2 TDP-43 (Figure 4D), it was tempting to propose that the two RRMs might function antagonistically to maintain the shape and the size of TDP-43 NBs. To test this hypothesis, we co-expressed HA-tagged WT TDP-43 with Myc-tagged WT, ΔRRM1, or ΔRRM2 TDP-43 and induced the NB formation in 293T cells by LMB (Figures 4E–4H). ΔRRM1 formed a ring-shaped shell wrapping the co-expressed WT TDP-43 NBs (Figures 4F and 4J), and the diameter of these NBs was larger (Figure 4N). The increased size was not simply due to OE of two folds of the TDP-43 protein, because co-expression of WT TDP-43-HA and WT Myc-TDP-43 did not show this effect (Figures 4E, 4I, and 4M). ΔRRM2 co-expressed with WT TDP-43 was mainly localized to the core (Figures 4G and 4K) and was a smaller size than WT TDP-43 NBs (Figure 4O). Similar results were obtained with co-expression of ΔRRM1 and ΔRRM2 (Figures 4H, 4L, and 4P).

Figure 1. TDP-43 Forms Reversible, Dynamic NBs in Response to Arsenic Stress

(A and B) Representative images (A) and quantifications (B) of HeLa cells forming TDP-43 NBs (arrows) and TDP-43^{+} SGs (arrowheads) induced by arsenite (250 μM, 30 min). TIAR, SG marker; DAPI, nuclear labeling. See also Video S1.

(C) Same as (A) but stained for endogenous TDP-43 (enTDP-43) by anti-TDP-43.

(D) The intensity profiles of enTDP-43 along the indicated lines in (C).

(E) Quantification of % of cells with enTDP-43 NBs in (C).

(F and G) FRAP analysis of GFP-TDP-43 NBs in *live* cells induced by arsenite treatment for 30 min (F) or 6 h (G). See also Video S2.

(H) The FRAP recovery curves of (F) and (G) are quantified (see STAR Methods).

(I–L) Confocal images (I) and quantifications (J–L) of the dynamics of TDP-43 NBs and TDP-43^{+} SGs in the washout assay.

Mean ± SEM; n = ~100 cells (B, E, J, and K), n = ~9 NBs (H), and n = ~15 cells (L) each group from pooled results of 3 independent repeats. Student's t test (B and E), two-way ANOVA (B and H), one-way ANOVA (J–L). Scale bars, 10 μm (A) and 5 μm (C, F, G, and I).

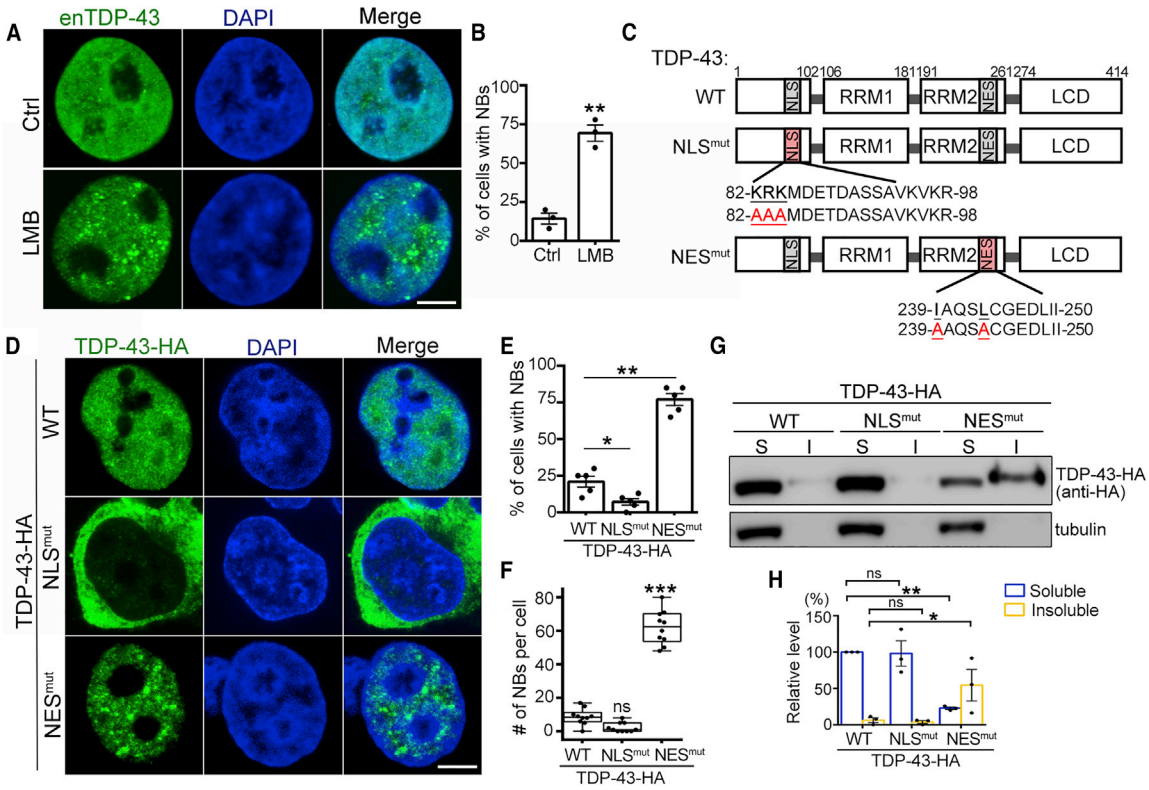

Figure 2. Inhibition of Nuclear Export Induces the Assembly of TDP-43 NBs

(A and B) Representative images (A) and quantifications (B) of enTDP-43 forming NBs upon LMB treatment (45 nM, 18 h).

(C) A diagram of the major domains and the residues mutated in human TDP-43 in this figure.

(D–F) Confocal images (D) and quantifications (E and F) of the NBs formed by WT, NLS^{mut}, or NES^{mut} TDP-43.

(G and H) Western blot analysis of WT, NLS^{mut}, and NES^{mut} TDP-43 proteins in the detergent-soluble (S) and insoluble fractions (I) (see STAR Methods).

Mean ± SE; n = ~120 cells (B and E), n = ~10 cells (F), and n = 3 repeats (G and H); ns, not significant. Student's t test (B) and one-way ANOVA (E, F, and H). Scale bars, 5 μm.

Next, we examined the co-localization of the above TDP-43 nuclear structures with PSs by co-immunostaining of NONO, a PS protein known to reside in the core of PSs (West et al., 2016). Consistently, NONO showed up in the core of WT and ΔRRM2 TDP-43 NBs (Figures 4Q and 4S). Interestingly, the ring-shaped ΔRRM1 did not co-localize with PSs labeled by NONO (Figure 4R), suggesting that TDP-43 requires the RRM1 to be associated with PSs and that TDP-43 NBs are not homogeneous, although a significant subpopulation overlapped with PSs (Figure S1). Together, these data indicate that the two RRMs play distinct functions in the assembly and maintenance of TDP-43 NBs, possibly by interacting with different RNAs and/or RBPs.

RNA Suppresses TDP-43 *In Vitro* De-mixing via the RRMs

The dynamic and reversible characteristics of TDP-43 NBs suggested that LLPS might underlie the NB formation. Purified full-length (FL) TDP-43 protein formed LDs *in vitro* in a dose-dependent manner, and the LCD played a significant role in promoting TDP-43 LLPS (Figures S6A–S6D). Nevertheless, *in vitro* de-mixing of the C-terminal LCD truncation (TDP-43$^{1-274}$) was evident at higher concentrations (≥50 μM) (Figure S6D), which was consistent with the previous report that the N-terminal domains of TDP-43 drove LLPS *in vivo* (Schmidt and Rohatgi, 2016). Next, we examined how RNA impacted TDP-43 LLPS by adding total RNAs extracted from HeLa cells into the *in vitro* de-mixing system (Figures S6E and S6F). Total RNAs (500 ng/μl) markedly reduced the LLPS of FL TDP-43 (Figure S6E), whereas much lower concentrations of RNAs (≥100 ng/μl) were sufficient to suppress the LLPS of TDP-43$^{1-274}$ (Figure S6F). Of note, the LCD made purified TDP-43 proteins extremely insoluble, for which a solubilizing sumo tag was needed to prevent the proteins from precipitation *in vitro*. With the sumo tag, however, it was tricky to form large sumo-TDP-43 droplets (Figures S6G–S6I), making it difficult to compare the two RRMs in RNA suppression. Hence, we used the TDP-43$^{1-274}$ protein that did not require the sumo tag to stay soluble (Figures S6J–S6L and 5A–5N) in the subsequent experiments.

To facilitate the evaluation, we lowered the NaCl concentration and increased the crowding agent PEG, which allowed larger TDP-43 LDs to form at the beginning of the suppression assay (Figures 5B–5D). Total RNAs (100 ng/μl) markedly reduced the size and the number of WT TDP-43$^{1-274}$ LDs (Figure 5B).

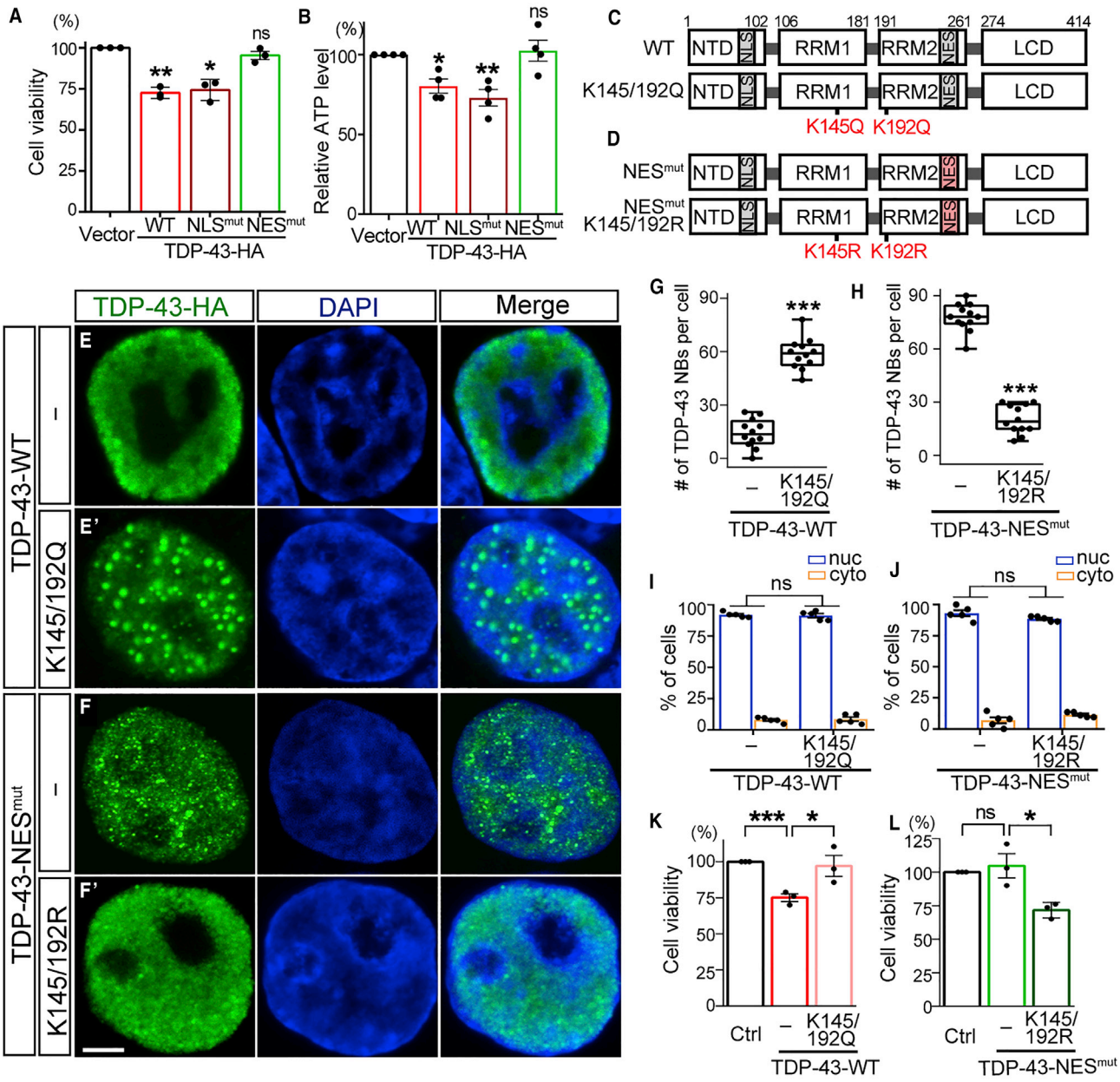

Figure 3. Formation of NBs Mitigates TDP-43-Mediated Cytotoxicity

(A) In the absence of stress, OE of WT or NLS^{mut}, but not NES^{mut}, TDP-43 is sufficient to decrease the cell viability.

(B) Relative ATP levels of 293T cells transfected with WT, NLS^{mut}, or NES^{mut} TDP-43.

(C and D) Diagrams showing the K145/192Q and K145/192R mutations.

(E–F′) Representative images of WT (E) and "WT + K145/192Q" TDP-43 (E′) or NES^{mut} (F) and "NES^{mut} + K145/192R" TDP-43 (F′) in 293T cells.

(G and H) Quantification of TDP-43 NB counts per cell in (E–F′) as indicated.

(I and J) Quantification of percentages of cells showing TDP-43 exclusively in the nucleus (nuc) or in both the nucleus and the cytoplasm (cyto) in (E–F′).

(K and L) K145/192Q suppresses whereas K145/192R enhances TDP-43 cytotoxicity.

Mean ± SEM; n = 3∼4 repeats (A, B, K, and L), n = ∼12 cells (G and H), and n = over 100 cells (I and J); ns, not significant. One-way ANOVA (A and B), Student's t test (G, H, K, and L), and two-way ANOVA (I and J). Scale bar, 5 μm.

ΔRRM1 TDP-43$^{1-274}$ (50 μM) only formed small LDs (Figure 5C), which initially made us presume that total RNAs would more easily suppress the LLPS of ΔRRM1. To our surprise, a much higher concentration of total RNAs (≥500 ng/μl) was required (Figure 5C). We also tested ΔRRM1 at a higher concentration (100 μM) to allow large ΔRRM1 LDs to form at the beginning, which confirmed the drastically reduced RNA suppression of the LLPS of ΔRRM1 TDP-43$^{1-274}$ (≥250 ng/μl) (Figure 5C′).

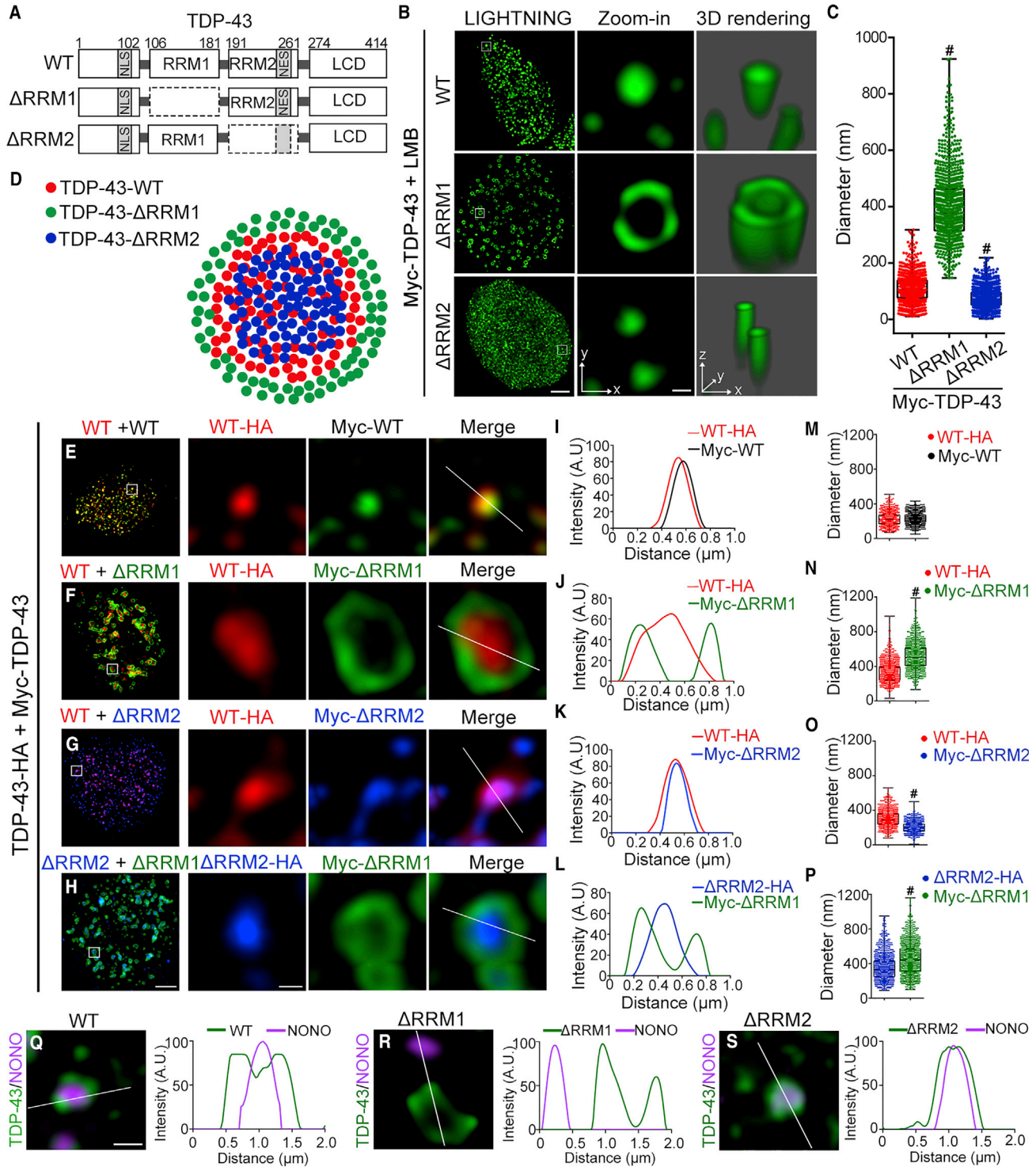

Figure 4. The RRM1 and RRM2 Function Complementarily in the Assembly and Maintenance of TDP-43 NBs

(A) A diagram of WT, ΔRRM1 and ΔRRM2 TDP-43.

(B and C) LIGHTNING super-resolution microscopy (B) and quantification of the diameters (C) of LMB-induced NBs formed by WT, ΔRRM1, or ΔRRM2 TDP-43 in 293T cells. Zoom-ins and 3D renderings are shown.

(D) A model representing the TDP-43 NB with different RRM deletions.

(E–H) Multicolor super-resolution microscopy and zoom-in images of LMB-induced WT+WT (E), WT+ΔRRM1 (F), WT+ΔRRM2 (G), and ΔRRM1+ΔRRM2 (H) TDP-43 NBs.

(legend continued on next page)

The RNA suppression of the LLPS of ΔRRM2 TDP-43$^{1-274}$ was also reduced but to a lesser extent than that of ΔRRM1 (100∼250 ng/μl) (Figure 5D). The dot-blot assay confirmed reduced RNA-binding affinity in both ΔRRM1 and ΔRRM2 TDP-43$^{1-274}$ (Figures S6M–S6O). These data indicate that an RBP with lower tendency to phase separate does not necessarily mean RNAs would more readily suppress its LLPS. Instead, the regulation by RNAs is rather specific, likely depending on the type and content of the RNAs.

tRNA reduced the LLPS of FUS *in vitro* (Maharana et al., 2018), which also potently suppressed *in vitro* de-mixing of TDP-43 in this study (Figure 5E). WT and ΔRRM1 TDP-43$^{1-274}$ showed similar sensitivity to tRNA (≥1.25 μg/μl) (Figures 5E and 5F), whereas ΔRRM2 required a higher concentration of tRNA (≥2.5 μg/μl) (Figure 5G). Unlike total RNAs, ΔRRM1 TDP-43$^{1-274}$ did not exhibit a greatly decreased sensitivity to tRNA suppression (Figures 5C and 5F). Thus, the lack of a strong suppression of the LLPS of ΔRRM1 by total RNAs was not simply because suppression of small LDs was difficult to manifest or detect. Together, RRM1 appeared to play a major role in mediating the suppression of TDP-43 LLPS by total RNAs, whereas RRM2 might be more involved in the suppression by tRNA.

LncRNA *NEAT1* Promotes TDP-43 LLPS and Is Upregulated in Stressed Neurons

Recent works have revealed both positive and negative regulation of protein LLPS by RNAs (Guo and Shorter, 2015). We found that the PS scaffolding RNA *NEAT1* not only directly bound to TDP-43 protein *in vitro* (Figure 5H) but also promoted TDP-43 de-mixing in a dose-dependent manner (Figure 5I), which involved both RRM1 and RRM2 (Figures 5J and 5K). Furthermore, we demonstrated that increasing concentrations of *NEAT1* antagonized the suppressive environment generated by tRNA in the *in vitro* LLPS assay of TDP-43 (Figure 5L), which was markedly reduced by ΔRRM1 but enhanced by ΔRRM2 (Figures 5M and 5N). These data suggest that, in the nucleoplasm that contains both positive and negative regulatory RNAs, the RRM1 may play a major role in mediating *NEAT1*-promotion of TDP-43 LLPS, whereas the RRM2 may be more involved in the tRNA-mediated suppression.

In addition, we examined TDP-43-NES^{mut}, and its RNA-binding affinity was significantly reduced (Figures S3H and S3I), which was consistent with the previous studies (Lukavsky et al., 2013; Flores et al., 2019). Moreover, the K145/192Q mutation also impaired RNA binding (Figures S3F and S3G) and reduced the suppression of TDP-43 LLPS by total RNAs (Figures S3J–S3L). The K145/192R mutation did not increase RNA binding (Figures S3F–S3I) or enhance the total RNA suppression (Figure S3L). Instead, it disrupted *NEAT1*-mediated TDP-43 droplet formation (Figures S3M–S3O), which might complement the lack of RNA suppression in the NES^{mut}. As such, TDP-43-NES^{mut}-K145/192R did not form NBs spontaneously (Figures 3F, 3F′ and 3H) and regained cytotoxicity (Figure 3L).

Next, we extended our investigation of TDP-43 NBs and *NEAT1* to neurons. Consistently, TDP-43 formed NBs in mouse primary neurons upon stress (Figures 5O, 5O′, 5R, and 5U); ΔRRM1 TDP-43 formed large, ring-shaped structures in both normal and stressed mouse neurons (Figures 5P, 5P′, and 5S); ΔRRM2 displayed a grainy appearance when stressed (Figures 5Q, 5Q′, and 5T). More importantly, the levels of both total *NEAT1* RNA and the lncRNA isoform *NEAT1_2* were dramatically increased in stressed mouse neurons (Figures 5V and 5W). These data suggest that stress triggers the upregulation of *NEAT1* RNA, which provides nucleation scaffolds to condense TDP-43 (and possibly other NB components) and promote the LLPS, leading to the formation of TDP-43 NBs.

ALS-Associated D169G Mutation of TDP-43 Shows a Specific Defect in NB Formation

To investigate the disease relevance of TDP-43 NBs, we then examined several known ALS-causing mutations in TDP-43. We found that a mutation of D169G (640A→T) within the RRM1 (Kabashi et al., 2008; Figures 6A and 6B) drastically reduced the stress-induced assembly of TDP-43 NBs (Figures 6C–6E; Figures S7A–S7C). In contrast, the formation of SGs or the recruitment of TDP-43-D169G to SGs was not reduced (Figures 6C and 6F). Unlike TDP-43-D169G, the disease-associated mutations in the LCD, such as Q331K and M337V, did not hinder the NB formation (Figures S7D–S7G). Thus, although TDP-43 NBs and SGs are both phase-separated, membraneless RNP granules, the exact mechanisms regulating their formation may be different.

With extended arsenite treatment (250 μM, 120 min), D169G eventually formed TDP-43 NBs (Figures 6C–6E). Surprisingly, we saw staggeringly more cells forming TDP-43^{+} SGs in D169G (75.6% ± 3.8%) than WT TDP-43 (31.3±2.3%) at this condition (Figures 6C and 6F). Phosphorylation of TDP-43 (pTDP-43) at S409/410 (pS409/410) is a disease-specific marker of TDP-43 aggregates (Hasegawa et al., 2008; Neumann et al., 2009). With prolonged stress (arsenite 250 μM, 6 h), the NB-forming defective D169G accumulated cytoplasmic foci that were positive for pS409/410, which was not observed with WT TDP-43 at the same condition (Figures 6G–6I). Of note, D169G in the nucleus was absent of pS409/410 staining even with prolonged stress (Figure 6H), indicating that TDP-43-D169G was not generally hyperphosphorylated but only so when the abnormal cytoplasmic foci formed. Moreover, D169G caused significantly more cell death during mild but prolonged stress (arsenite 100 μM, 12 h) (Figures 6J–6K′). These results suggest that the assembly of TDP-43 NBs upon stress might lower the demand for cytoplasmic translocation and participation of TDP-43 in SGs, therefore reducing the chance of aberrant phase transition and

(I–L) The intensity profiles along the indicated lines across the NBs in (E–H).
(M–P) The diameters of the different TDP-43 NBs in (E–H) are quantified.
(Q–S) Super-resolution images and intensity line analyses of WT (Q), ΔRRM1 (R), and ΔRRM2 (S) TDP-43 NBs (green) co-immunostained with the PS marker NONO (purple).
The box-and-whisker plots with values and n = ∼900 NBs (C and M–P). $^{\#}p < 0.0001$. One-way ANOVA (C) and Student's t test (M–P). Scale bars, 5 μm (B), 2 μm (E–H), 500 nm (Q–S), and 200 nm in the zoom-ins (B and E–H).

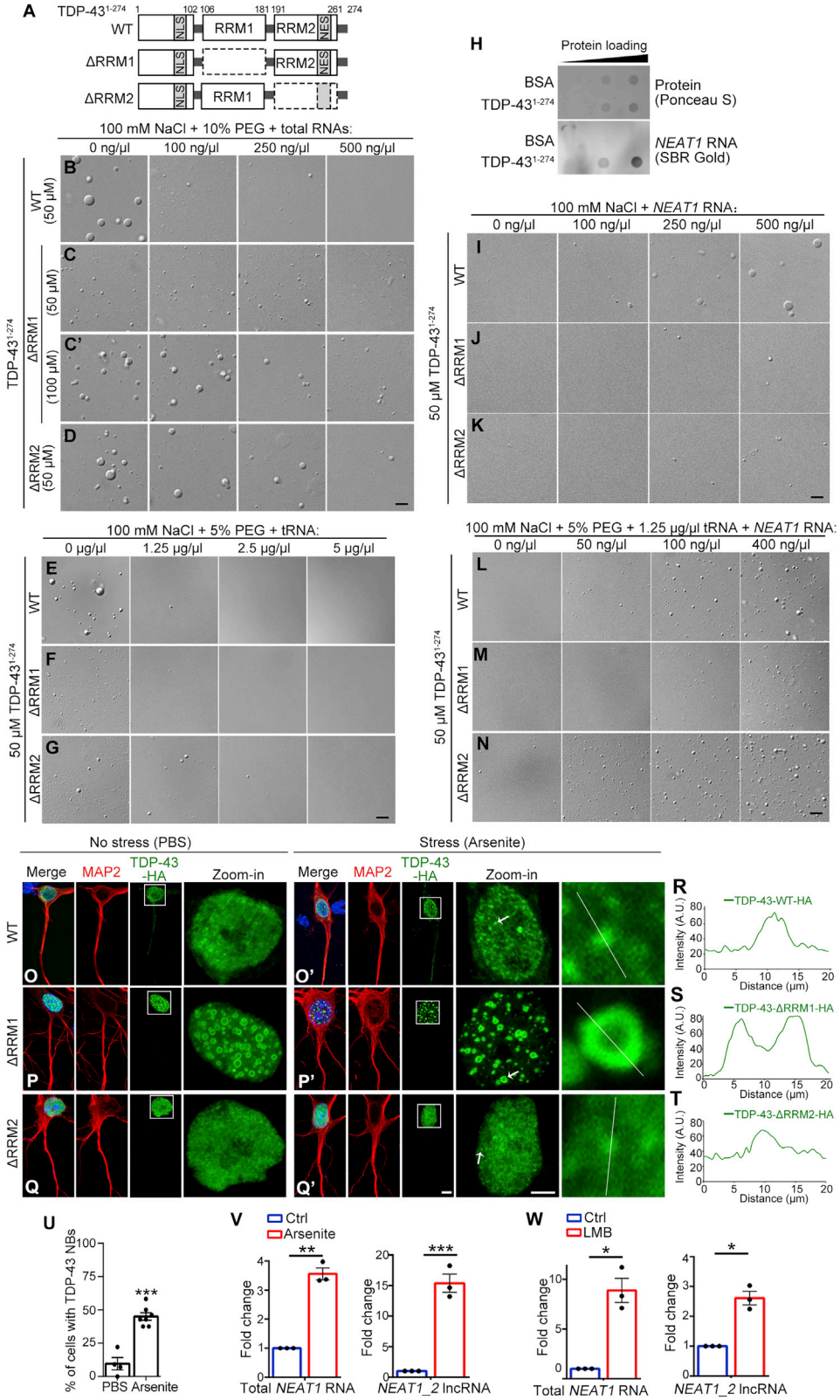

(legend on next page)

accumulation of pathogenic pTDP-43 inclusions in the cytoplasm.

To assess the neurotoxicity of D169G in *in vivo* settings, we generated transgenic flies expressing hTDP-43-D169G (Figures 6L and 6M). These flies exhibited eye degeneration during aging (Figure 6N), and the enhanced toxicity was more evident when D169G was expressed in fly motor neurons: the climbing capability showed an accelerated decline compared to flies expressing WT hTDP-43 (Figure 6O). Aging is associated with cumulative stress and is a risk factor for neurodegenerative diseases (López-Otín et al., 2013; Hou et al., 2019). Thus, these data further support the idea that the D169G mutation makes cells more prone to stress, which may underlie its pathogenesis in ALS disease.

The D169G Mutation Diminishes LncRNA *NEAT1*-Mediated TDP-43 LLPS *In Vitro* and NB Formation in Cells

To understand the molecular basis for the NB-forming deficit of D169G, we examined the phase behaviors of TDP-43-D169G in the *in vitro* LLPS assay. D169G formed LDs in a dose-dependent manner similar to WT TDP-43$^{1-274}$ (Figures 7A and 7B), indicating that the ability of D169G to phase separate was not reduced. Neither was the binding affinity of D169G to total RNAs (Figures S7H–S7J). Suppression of TDP-43 LLPS by total RNAs showed no marked difference between D169G and WT TDP-43$^{1-274}$ (Figures 7C and 7D). Thus, the general regulation of TDP-43 droplets by total RNAs remained intact in D169G.

In contrast, the induction of TDP-43 LLPS by *NEAT1* RNA was drastically reduced by D169G (Figures 7E and 7F). The RNA electrophoretic mobility shift assay (EMSA) showed that incubation with TDP-43 proteins markedly slowed down the migration speed of *NEAT1* RNA, leading to a dose-dependent band shift (Figure 7G). The band shifts caused by D169G were less robust than WT TDP-43 (Figures 7G and 7H), indicating reduced binding of D169G to *NEAT1* RNA. We did notice that at a higher protein concentration (16 μM), the difference between D169G and WT TDP-43 became smaller. This again points to the importance of the relative RNA and protein concentrations in regulating TDP-43 NBs, which may partially explain why the stress-induced NB formation was delayed, but not completely abolished, by D169G (Figures 6C–6E).

Finally, we conducted fluorescence *in situ* hybridization (FISH) for *NEAT1* lncRNA together with immunostaining for TDP-43-HA in HeLa cells. Stress significantly increased the colocalization of *NEAT1* lncRNA foci with WT TDP-43 NBs (Figures 7I, 7J, 7M, and 7N), which was not observed with D169G (Figures 7K, 7L, 7O, and 7P), suggesting that *NEAT1* lncRNA was unable to nucleate D169G to form NBs in cells. To further confirm the requirement of *NEAT1* in the assembly of TDP-43 NBs, we downregulated *NEAT1* by small interfering RNA (siRNA) (Figures 7Q and 7R). Knockdown (KD) of *NEAT1* dramatically reduced the numbers of stress-induced *NEAT1* puncta, as well as TDP-43 NBs (Figures 7S–7X). Together, the PS scaffolding lncRNA *NEAT1* mediated the assembly of stress-induced TDP-43 NBs

DISCUSSION

The Stress-Induced TDP-43 NB and its Cytoprotective Function

We show in this study that various cellular stresses trigger the formation of dynamic, reversible TDP-43 NBs. They are observed in human cells, mouse primary neurons, and *Drosophila* brains *in vivo*. Similarly, a recent paper by Gasset-Rosa et al. (2019) showed that TDP-43 at its endogenous level forms nuclear droplets in multiple cell types. Thus, the assembly of TDP-43 NBs occurs in various cell types and in different organisms, suggesting a general role and wide participation of TDP-43 NBs in response to stress.

We show in this study that the NB-forming NES^{mut} and K145/192Q TDP-43 are less cytotoxic than diffused WT TDP-43, and disruption of the NB formation abolishes the toxicity-mitigating effect. How do TDP-43 NBs acquire cytoprotection? It is thought that SGs help cells survive stress by sequestering mRNAs and temporarily arresting protein synthesis (Liu-Yesucevitz et al., 2010). Given the presence of TDP-43 in both SGs and TDP-43 NBs, it is conceivable that a similar mechanism may underlie the cytoprotective function of TDP-43 NBs. For example, the assembly of TDP-43 NBs may stall DNA transcription and/or arrest RNA processing in stressed cells; when stress is relieved, TDP-43 NBs disassemble, releasing RNAs and nuclear proteins for normal cellular functions. During prolonged stress, however, TDP-43 NBs become irreversible protein aggregates, which is consistent with the observation of intranuclear inclusions of TDP-43 in some ALS cases (Forman et al., 2007). In addition,

Figure 5. *NEAT1* RNA Promotes TDP-43 LLPS *In Vitro* and Is Upregulated in Stressed Neurons

(A) A diagram of WT, ΔRRM1, and ΔRRM2 of TDP-43$^{1-274}$.

(B–D) *In vitro* LLPS assay of WT (B), ΔRRM1 (C and C′), and ΔRRM2 (D) TDP-43$^{1-273}$ with total RNA extracts added as indicated. (C′) A higher concentration of ΔRRM1 with large LDs as WT TDP-43 is also tested. The concentrations of NaCl, the crowding agent PEG, TDP-43 proteins, and RNAs used in the *in vitro* assays are indicated.

(E–G) *In vitro* LLPS of WT (E), ΔRRM1 (F), and ΔRRM2 (G) TDP-43$^{1-273}$ with tRNA.

(H) The *in vitro* dot-blot assay confirming direct binding of *NEAT1* RNA to TDP-43. Bovine serum albumin (BSA) is used as a negative binding control.

(I–K) *In vitro* LLPS of WT (I), ΔRRM1 (J), and ΔRRM2 (K) TDP-43$^{1-273}$ with *NEAT1* RNA.

(L–N) *NEAT1* RNA antagonizes tRNA-mediated suppression of WT (L), ΔRRM1 (M), and ΔRRM2 (N) TDP-43 LLPS.

(O–Q′) Representative images of mouse primary neurons expressing WT (O and O′), ΔRRM1 (P and P′), and ΔRRM2 (Q and Q′) TDP-43 treated with PBS or arsenite as indicated. MAP2, neuronal marker.

(R–T) Intensity line analyses of the TDP-43 NBs indicated by the arrows in the zoom-ins in (O′–Q′).

(U) Quantification of % of neurons showing WT TDP-43 NBs in (O and O′), n = ~100.

(V and W) Stress induced by arsenite (V) or LMB (W) increases the levels of total *NEAT1* RNA and the *NEAT1_2* isoform in mouse primary neurons, n = 3. Mean ± SEM; Student's t test. Scale bars, 2 μm (B–G and I–N), 5 μm (O–Q′) and 2 μm in the zoom-ins.

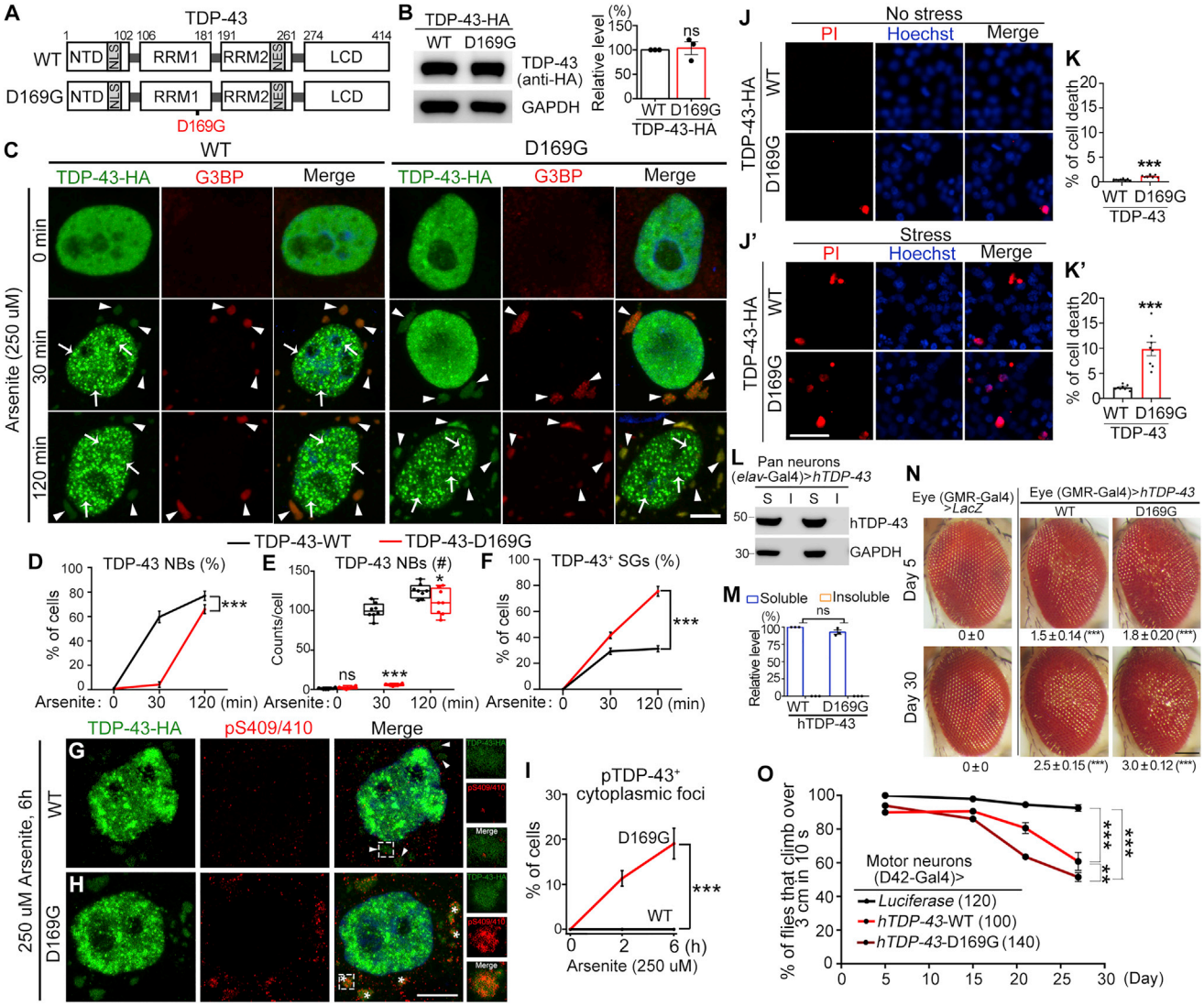

Figure 6. TDP-43-D169G Impairs NB Assembly, Accumulates Pathological Cytoplasmic Foci and Potentiates the Cytotoxicity of TDP-43 in Prolonged Stress and Aging

(A) A diagram showing WT and D169G mutant TDP-43.

(B) Western blot analysis of WT and D169G TDP-43 in HeLa cells.

(C) Confocal images of HeLa cells transfected with WT or D169G TDP-43 and treated with arsenite for indicated durations. G3BP, a SG Marker. Arrows, TDP-43 NBs; arrowheads, TDP-43^{+} SGs.

(D–F) Quantifications of percentages of cells showing TDP-43 NBs (D), TDP-43 NB counts per cell (E), and percentages of cells showing TDP-43^{+} SGs (F) in (C).

(G–I) Representative images (G and H) and quantification (I) of cells transfected with WT or D169G TDP-43-HA showing pS409/410^{+}-TDP-43 cytoplasmic foci during prolonged arsenic stress (250 μM, 6 h). TDP-43-HA (green), pS409/410 (red), and DAPI (blue). Arrowheads, TDP-43^{+} SGs; asterisks, pTDP-43^{+} cytoplasmic foci.

(J and J′) Cell death analysis of WT or D169G TDP-43 by PI staining in the absence (J) or presence (J′) of prolonged arsenic stress. Hoechst, nuclear labeling.

(K and K′) Quantifications of percentages of cells showing positive PI staining in (J and J′).

(L and M) Western blot analysis of the protein levels and solubility of hTDP-43-D169G in transgenic flies. S, soluble; I, insoluble.

(N) Fly eyes expressing WT or D169G hTDP-43 (GMR-Gal4) at indicated ages. The degeneration scores (mean ± SEM) and the statistical significance compared to the control flies (UAS-*lacZ*) are indicated.

(O) The climbing assay of the flies expressing WT or D169G hTDP-43 in motor neurons (D42-Gal4), number of flies tested in each group are indicated.

Mean ± SEM; n = 3 repeats (B and M), n = ~100 cells (D, F, and I), n = ~8 cells (E), n = ~2000 cells (K and K′), n = 13~16 fly eyes (N) in each group; ns, not significant. Student's t test (B, E, K, K′, and M), one-way ANOVA (N) and two-way ANOVA (D, F, I, and O). Scale bars, 5 μm (C, G, and H), 50 μm (J), and 100 μm (N).

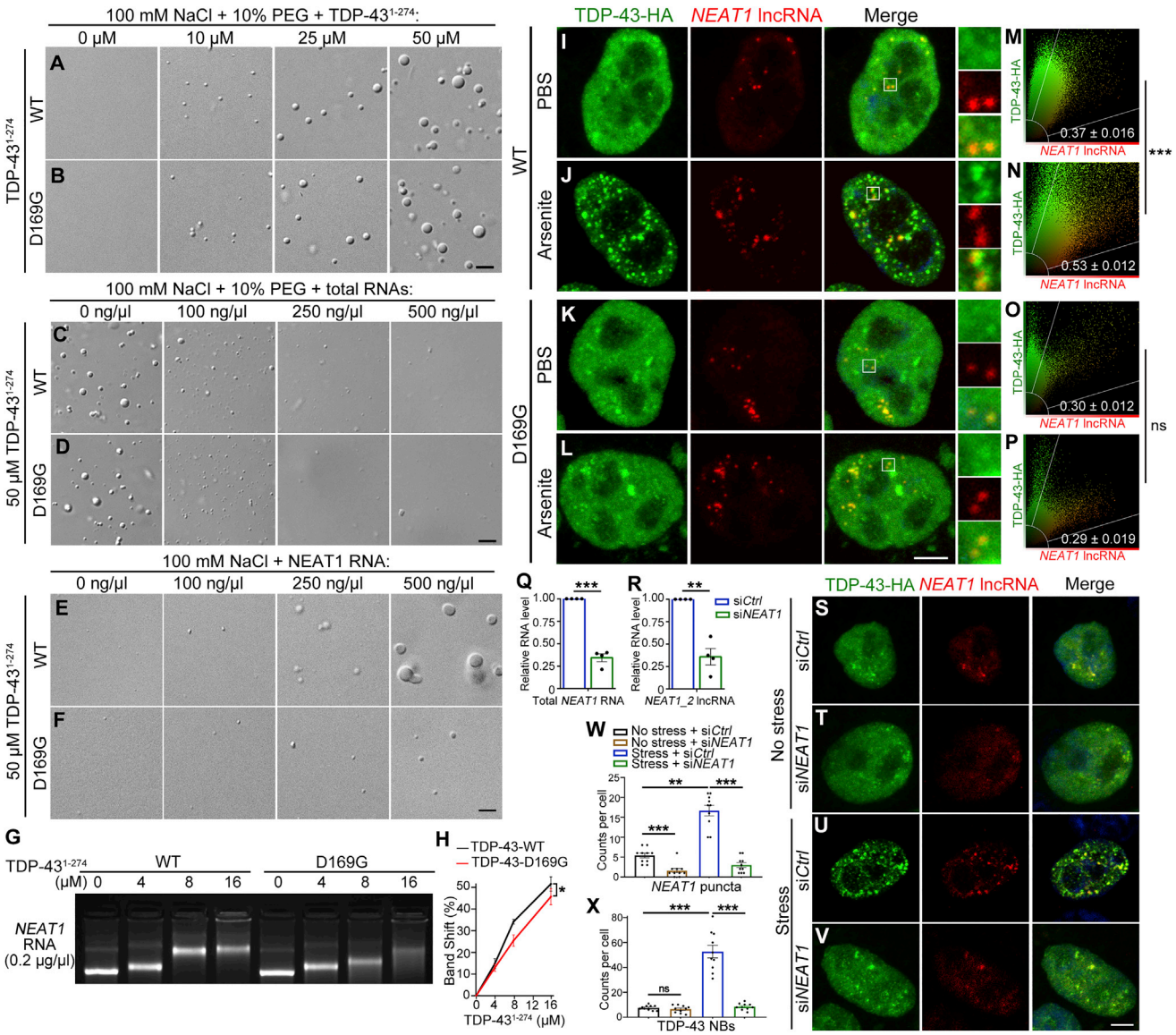

Figure 7. D169G Impairs the *NEAT1*-Mediated Nucleation of TDP-43 Droplets

(A and B) Both WT (A) and D169G (B) TDP-43 form LDs by LLPS in a dose-dependent manner.

(C and D) Total RNAs suppress *in vitro* LLPS of WT (C) and D169G (D) TDP-43.

(E and F) *NEAT1* promotion of WT (E) TDP-43 LLPS is dramatically reduced by D169G (F).

(G and H) Representative image (G) and quantification (H) of the EMSA gel shift assay of *NEAT1* RNA incubated with WT or D169G TDP-43$^{1-274}$ protein.

(I–L) Confocal images WT (I and J) or D169G (K and L) TDP-43 NBs in the absence or presence of stress as indicated, co-stained for *NEAT1* lncRNA by FISH in HeLa cells.

(M–P) Colocalization of TDP-43-HA and *NEAT1* lncRNA in the cells in (I–L) is assessed by Pearson's correlation coefficient of the fluorescence intensity of each channel for all pixels and shown on the right of each group.

(Q and R) Relative levels of total *NEAT1* RNA (Q) and the *NEAT1_2* isoform (R) with *NEAT1* siRNA (si*NEAT1*) determined by qPCR.

(S–V) Representative images of *NEAT1* RNA puncta and TDP-43 NBs in cells in the absence (S and T) or presence (U and V) of stress, treated with si*Ctrl* or si*NEAT1* as indicated.

(W and X) Quantifications of the number of *NEAT1* puncta (W) or TDP-43 NBs (X) in (S–V).

Mean ± SEM; n = 4 repeats (H and Q–R), n = ~20 cells (M–P), and n = ~10 cells (W and X); ns, not significant. Two-way ANOVA (H) and Student's t test (M–R, W, and X). Scale bars, 2 μm (A–F) and 5 μm (I–L and S–V).

given that the cellular levels of poly(ADP-ribose) (PAR) regulate the dynamics of SGs containing TDP-43 (McGurk et al., 2018; Duan et al., 2019) and that poly(ADP-ribose) polymerases (PARPs) are enriched in the nucleus (Hottiger, 2015), it will be interesting to investigate the role of PAR and PARPs in the formation of TDP-43 NBs in the future.

The Organization of TDP-43 NBs and the Functions of the Two RRMs

TDP-43 contains two canonical RRMs in tandem. RRM1 has a longer Loop3 region than RRM2 and is thought to have a higher affinity for RNAs (Buratti and Baralle, 2001; Kuo et al., 2014). Although ΔRRM1 and ΔRRM2 show similar binding affinity to total RNAs, they do display divergent responses to RNAs in the *in vitro* LLPS assays. For example, suppression of TDP-43 LLPS by total RNAs is greatly reduced by ΔRRM1 but only slightly decreased by ΔRRM2; in the assay, using tRNA to mimic nucleoplasmic suppression, the promotion of TDP-43 LLPS by *NEAT1* RNA is much reduced by ΔRRM1 but increased by ΔRRM2.

The RRM1 appears to have two seemingly conflicting functions: suppressing TDP-43 phase separation by total RNAs under normal conditions and mediating *NEAT1* RNA nucleation and condensation of NBs when TDP-43 LLPS is induced. In contrast, since ΔRRM2 retains the suppression by total RNAs mediated by the RRM1, it does not spontaneously phase separate. When TDP-43 LLPS is triggered by cellular stress, however, the RRM2-mediated "centrifugal force" is missing, and ΔRRM2 cannot counteract the RRM1 and *NEAT1*-mediated "centripetal force," which is therefore condensed to small, insoluble NBs. The distinct roles of the two RRMs in regulating the assembly of TDP-43 NBs likely result from different RNA-recognition patterns and binding preferences. Supporting this idea, the RRM1 mediates the promotion of TDP-43 LLPS by *NEAT1* lncRNA, whereas the RRM2 is more involved in the suppression by tRNA.

The Role of LncRNA *NEAT1* in the Assembly of TDP-43 NBs

LncRNAs are thought to provide the scaffold for the assembly of PSs (Clemson et al., 2009; Chen and Carmichael, 2009; Yamazaki et al., 2018). In particular, the lncRNA *NEAT1* is increased in patients and/or animal models of several neurodegenerative diseases, including ALS (Nishimoto et al., 2013), Alzheimer's disease (Puthiyedth et al., 2016), Parkinson's disease (Mariani et al., 2016), Huntington's disease (Cheng et al., 2018), and multiple sclerosis (Schirmer et al., 2019).

In this study, we find that *NEAT1* lncRNA is upregulated in stressed neurons and mediates the nucleation of TDP-43 NBs. As *NEAT1* lncRNA is over 20 kb in length and has complex secondary structures, we speculate that it may provide multiple binding sites for gathering TDP-43 molecules (and potentially other *NEAT1*-binding proteins). This would increase the multivalent interactions leading to co-phase separation of TDP-43 and *NEAT1*. In contrast, shorter RNAs, such as tRNA, which lack long stretches to accommodate multiple TDP-43 molecules, may instead segregate each individual TDP-43, therefore suppressing LLPS. It is worth noting that *NEAT1* is an RNA target of TDP-43 (Polymenidou et al., 2011; Chung et al., 2018; Modic et al., 2019), implying complicated cross-regulations between TDP-43 and *NEAT1*, as well as between SGs and PSs (An et al., 2019b).

The D169G Mutation and the Relevance of TDP-43 NBs in ALS Pathogenesis

More than 30 disease-causing mutations have been identified in TDP-43, and most of them are in the LCD and adjacent regions (Chen-Plotkin et al., 2010; Lee et al., 2011). D169G is the only known ALS-causing mutation in the RRM1 of TDP-43 (Kabashi et al., 2008), and its pathogenic mechanism had been elusive. It was presumed to abrogate RNA binding due to its location within the RRM (Kabashi et al., 2008); however, it turns out that D169G only causes a small local conformational change in the Turn6 of the β sheets within the RRM1 without reducing the overall binding affinity of TDP-43 to RNA or DNA (Austin et al., 2014; Kuo et al., 2014; Chiang et al., 2016). And, although D169G exhibits slightly increased thermal stability and may be more susceptible to proteolytic cleavage (Austin et al., 2014; Chiang et al., 2016), it does not engender aberrant oligomerization but instead increases the resistance of TDP-43 to aggregation (Austin et al., 2014). The only known major alteration by D169G is that it reduces polyubiquitination and co-aggregation of TDP-43 with Ubiquilin 1 (Kim et al., 2009). However, given the long-standing notion that cytoplasmic inclusions containing ubiquitinated TDP-43 are a pathological hallmark and cause of the disease (Li et al., 2013; Zhao et al., 2018), it has been difficult to understand how decreased ubiquitination and aggregation of TDP-43-D169G lead to ALS.

In this study, we discovered that D169G has a striking and specific deficit in the assembly of stress-induced TDP-43 NBs, which is caused by reduced *NEAT1* RNA-binding and nucleation. More interestingly, the NB-defective D169G forms significantly more TDP-43^{+} SGs in prolonged stress, giving rise to hyperphosphorylated cytoplasmic TDP-43 foci. Together, we propose that the stress-induced upregulation of *NEAT1* lncRNA promotes the assembly of TDP-43 NBs via LLPS, which is called up to engage in the first line of defense against stress and disease conditions. Prompt assembly of TDP-43 NBs lowers the need to form cytoplasmic SGs, preventing excessive cytoplasmic accumulation of TDP-43. The ALS-causing D169G mutation diminishes the assembly of TDP-43 NBs and forms abnormal cytoplasmic foci containing pTDP-43 in prolonged stress, which may contribute to ALS pathogenesis. Given that cytoplasmic mislocalization and nuclear depletion of TDP-43 are common in diseased neurons, it is likely that loss of the TDP-43 NB-mediated stress-mitigating mechanism may also underlie other ALS cases and related diseases.

STAR★METHODS

Detailed methods are provided in the online version of this paper and include the following:

- KEY RESOURCES TABLE
- RESOURCE AVAILABILITY
  - Lead Contact
  - Materials Availability
  - Data and Code Availability
- EXPERIMENTAL MODEL AND SUBJECT DETAILS
  - *Drosophila* strains and husbandry
  - Mouse care and primary neuron culture
- METHOD DETAILS
  - Plasmids and constructs
  - Lentivirus production
  - Cell cultures and transfection
  - Pharmacological assays

- Immunocytochemistry and immunohistochemistry
- Confocal and super-resolution imaging
- Live cell imaging
- FRAP assay
- Antibodies
- Protein extraction and western blotting
- Cell viability assay
- ATP level measurement
- RNA extraction and real-time quantitative PCR
- Purification of TDP-43 proteins
- Dot-blot RNA-protein binding assay
- *In vitro* phase separation and RNA buffering assay
- Electrophoretic mobility-shift assay
- Fluorescence *in situ* hybridization
- Eye degeneration analysis and climbing assay in flies

● QUANTIFICATION AND STATISTICAL ANALYSIS

SUPPLEMENTAL INFORMATION

Supplemental Information can be found online at https://doi.org/10.1016/j.molcel.2020.06.019.

ACKNOWLEDGMENTS

We thank the BDSC for providing the fly strains, the SIBCB *Drosophila* Center for the fly embryo injection services, L. Chen, L. Pan, J. Zhou, and Z. Zhang for the vectors and plasmids, Z. Zhang for help in the pulse-chase assay, J. Yuan, A. Li, Y. Chen, and Z. He for comments and critical reading of the manuscript. This work is supported by grants from the National Key R&D Program of China (2016YFA0501902 to Y.F.), the National NSFC (81671254 and 31970697 to Y.F. and 91853112 and 31470748 to C.L.), the SMSTC Major Project (2019SHZDZX02 to Y.F. and C.L. and 18JC1420500 to C.L.), and the Alzheimer's Association (AARF-16-441196 to L.G.) and Target ALS Springboard Fellowship (to L.G.).

AUTHOR CONTRIBUTIONS

G.D., Z.M., and Y.F. conceived the research; C.W., Y.D., G.D., C.L., L.G., and Y.F. designed the experiments; C.W., Y.D., G.D., Q.W., K.Z., X.D., B.Q., J.G., and S.Z. performed the experiments; C.W., Y.D., G.D., Q.W., Z.M., J.G., and C.L contributed important new reagents; C.W., Y.D., G.D., and Y.F. analyzed the data and interpreted the results; C.W., Y.D., G.D., and Y.F. prepared the figures; and C.W., Y.D., G.D., C.L., and Y.F. wrote the paper. All authors read and approved the final manuscript.

DECLARATION OF INTERESTS

The authors declare no competing interests.

Received: December 1, 2019
Revised: May 1, 2020
Accepted: June 9, 2020
Published: July 9, 2020

SUPPORTING CITATIONS

The following references appear in the Supplemental Information: Fu and Maniatis (1990); Koken et al. (1994); Prasanth et al. (2005); and Santama et al. (2005).

REFERENCES

An, H., Skelt, L., Notaro, A., Highley, J.R., Fox, A.H., La Bella, V., Buchman, V.L., and Shelkovnikova, T.A. (2019a). ALS-linked FUS mutations confer loss and gain of function in the nucleus by promoting excessive formation of dysfunctional paraspeckles. Acta Neuropathol. Commun. *7*, 7.

An, H., Tan, J.T., and Shelkovnikova, T.A. (2019b). Stress granules regulate stress-induced paraspeckle assembly. J. Cell Biol. *218*, 4127–4140.

Archbold, H.C., Jackson, K.L., Arora, A., Weskamp, K., Tank, E.M., Li, X., Miguez, R., Dayton, R.D., Tamir, S., Klein, R.L., and Barmada, S.J. (2018). TDP43 nuclear export and neurodegeneration in models of amyotrophic lateral sclerosis and frontotemporal dementia. Sci. Rep. *8*, 4606.

Austin, J.A., Wright, G.S., Watanabe, S., Grossmann, J.G., Antonyuk, S.V., Yamanaka, K., and Hasnain, S.S. (2014). Disease causing mutants of TDP-43 nucleic acid binding domains are resistant to aggregation and have increased stability and half-life. Proc. Natl. Acad. Sci. USA *111*, 4309–4314.

Ayala, Y.M., Zago, P., D'Ambrogio, A., Xu, Y.F., Petrucelli, L., Buratti, E., and Baralle, F.E. (2008). Structural determinants of the cellular localization and shuttling of TDP-43. J. Cell Sci. *121*, 3778–3785.

Banani, S.F., Lee, H.O., Hyman, A.A., and Rosen, M.K. (2017). Biomolecular condensates: organizers of cellular biochemistry. Nat. Rev. Mol. Cell Biol. *18*, 285–298.

Barmada, S.J., Skibinski, G., Korb, E., Rao, E.J., Wu, J.Y., and Finkbeiner, S. (2010). Cytoplasmic mislocalization of TDP-43 is toxic to neurons and enhanced by a mutation associated with familial amyotrophic lateral sclerosis. J. Neurosci. *30*, 639–649.

Bateman, J.R., Lee, A.M., and Wu, C.T. (2006). Site-specific transformation of Drosophila via phiC31 integrase-mediated cassette exchange. Genetics *173*, 769–777.

Bond, C.S., and Fox, A.H. (2009). Paraspeckles: nuclear bodies built on long noncoding RNA. J. Cell Biol. *186*, 637–644.

Buratti, E., and Baralle, F.E. (2001). Characterization and functional implications of the RNA binding properties of nuclear factor TDP-43, a novel splicing regulator of CFTR exon 9. J. Biol. Chem. *276*, 36337–36343.

Cao, X., Wang, H., Wang, Z., Wang, Q., Zhang, S., Deng, Y., and Fang, Y. (2017). In vivo imaging reveals mitophagy independence in the maintenance of axonal mitochondria during normal aging. Aging Cell *16*, 1180–1190.

Chen, L.L., and Carmichael, G.G. (2009). Altered nuclear retention of mRNAs containing inverted repeats in human embryonic stem cells: functional role of a nuclear noncoding RNA. Mol. Cell *35*, 467–478.

Chen-Plotkin, A.S., Lee, V.M., and Trojanowski, J.Q. (2010). TAR DNA-binding protein 43 in neurodegenerative disease. Nat. Rev. Neurol. *6*, 211–220.

Cheng, C., Spengler, R.M., Keiser, M.S., Monteys, A.M., Rieders, J.M., Ramachandran, S., and Davidson, B.L. (2018). The long non-coding RNA NEAT1 is elevated in polyglutamine repeat expansion diseases and protects from disease gene-dependent toxicities. Hum. Mol. Genet. *27*, 4303–4314.

Chiang, C.H., Grauffel, C., Wu, L.S., Kuo, P.H., Doudeva, L.G., Lim, C., Shen, C.K., and Yuan, H.S. (2016). Structural analysis of disease-related TDP-43 D169G mutation: linking enhanced stability and caspase cleavage efficiency to protein accumulation. Sci. Rep. *6*, 21581.

Chung, C.Y., Berson, A., Kennerdell, J.R., Sartoris, A., Unger, T., Porta, S., Kim, H.J., Smith, E.R., Shilatifard, A., Van Deerlin, V., et al. (2018). Aberrant activation of non-coding RNA targets of transcriptional elongation complexes contributes to TDP-43 toxicity. Nat. Commun. *9*, 4406.

Clemson, C.M., Hutchinson, J.N., Sara, S.A., Ensminger, A.W., Fox, A.H., Chess, A., and Lawrence, J.B. (2009). An architectural role for a nuclear noncoding RNA: NEAT1 RNA is essential for the structure of paraspeckles. Mol. Cell *33*, 717–726.

Cohen, T.J., Hwang, A.W., Restrepo, C.R., Yuan, C.X., Trojanowski, J.Q., and Lee, V.M. (2015). An acetylation switch controls TDP-43 function and aggregation propensity. Nat. Commun. *6*, 5845.

Dominguez, D., Freese, P., Alexis, M.S., Su, A., Hochman, M., Palden, T., Bazile, C., Lambert, N.J., Van Nostrand, E.L., Pratt, G.A., et al. (2018). Sequence, Structure, and Context Preferences of Human RNA Binding Proteins. Mol Cell *70*, 854–867.e9.

Duan, Y., Du, A., Gu, J., Duan, G., Wang, C., Gui, X., Ma, Z., Qian, B., Deng, X., Zhang, K., et al. (2019). PARylation regulates stress granule dynamics, phase

separation, and neurotoxicity of disease-related RNA-binding proteins. Cell Res. *29*, 233–247.

Ederle, H., Funk, C., Abou-Ajram, C., Hutten, S., Funk, E.B.E., Kehlenbach, R.H., Bailer, S.M., and Dormann, D. (2018). Nuclear egress of TDP-43 and FUS occurs independently of Exportin-1/CRM1. Sci. Rep. *8*, 7084.

Fahrenkrog, B., and Harel, A. (2018). Perturbations in Traffic: Aberrant Nucleocytoplasmic Transport at the Heart of Neurodegeneration. Cells *7*, E232.

Feric, M., Vaidya, N., Harmon, T.S., Mitrea, D.M., Zhu, L., Richardson, T.M., Kriwacki, R.W., Pappu, R.V., and Brangwynne, C.P. (2016). Coexisting Liquid Phases Underlie Nucleolar Subcompartments. Cell *165*, 1686–1697.

Flores, B.N., Li, X., Malik, A.M., Martinez, J., Beg, A.A., and Barmada, S.J. (2019). An Intramolecular Salt Bridge Linking TDP43 RNA Binding, Protein Stability, and TDP43-Dependent Neurodegeneration. Cell Rep. *27*, 1133–1150.e8.

Forman, M.S., Trojanowski, J.Q., and Lee, V.M. (2007). TDP-43: a novel neurodegenerative proteinopathy. Curr. Opin. Neurobiol. *17*, 548–555.

Fox, A.H., and Lamond, A.I. (2010). Paraspeckles. Cold Spring Harb. Perspect. Biol. *2*, a000687.

Fox, A.H., Nakagawa, S., Hirose, T., and Bond, C.S. (2018). Paraspeckles: Where Long Noncoding RNA Meets Phase Separation. Trends Biochem. Sci. *43*, 124–135.

Fu, X.D., and Maniatis, T. (1990). Factor required for mammalian spliceosome assembly is localized to discrete regions in the nucleus. Nature *343*, 437–441.

Gasset-Rosa, F., Lu, S., Yu, H., Chen, C., Melamed, Z., Guo, L., Shorter, J., Da Cruz, S., and Cleveland, D.W. (2019). Cytoplasmic TDP-43 De-mixing Independent of Stress Granules Drives Inhibition of Nuclear Import, Loss of Nuclear TDP-43, and Cell Death. Neuron *102*, 339–357.e7.

Groth, A.C., Fish, M., Nusse, R., and Calos, M.P. (2004). Construction of transgenic Drosophila by using the site-specific integrase from phage phiC31. Genetics *166*, 1775–1782.

Guo, L., and Shorter, J. (2015). It's Raining Liquids: RNA Tunes Viscoelasticity and Dynamics of Membraneless Organelles. Mol. Cell *60*, 189–192.

Hasegawa, M., Arai, T., Nonaka, T., Kametani, F., Yoshida, M., Hashizume, Y., Beach, T.G., Buratti, E., Baralle, F., Morita, M., et al. (2008). Phosphorylated TDP-43 in frontotemporal lobar degeneration and amyotrophic lateral sclerosis. Ann. Neurol. *64*, 60–70.

Hennig, S., Kong, G., Mannen, T., Sadowska, A., Kobelke, S., Blythe, A., Knott, G.J., Iyer, K.S., Ho, D., Newcombe, E.A., et al. (2015). Prion-like domains in RNA binding proteins are essential for building subnuclear paraspeckles. J. Cell Biol. *210*, 529–539.

Hottiger, M.O. (2015). SnapShot: ADP-Ribosylation Signaling. Mol. Cell *58*, 1134–1134.e1.

Hou, Y., Dan, X., Babbar, M., Wei, Y., Hasselbalch, S.G., Croteau, D.L., and Bohr, V.A. (2019). Ageing as a risk factor for neurodegenerative disease. Nat. Rev. Neurol. *15*, 565–581.

Hyman, A.A., Weber, C.A., and Jülicher, F. (2014). Liquid-liquid phase separation in biology. Annu. Rev. Cell Dev. Biol. *30*, 39–58.

Kabashi, E., Valdmanis, P.N., Dion, P., Spiegelman, D., McConkey, B.J., Vande Velde, C., Bouchard, J.P., Lacomblez, L., Pochigaeva, K., Salachas, F., et al. (2008). TARDBP mutations in individuals with sporadic and familial amyotrophic lateral sclerosis. Nat. Genet. *40*, 572–574.

Kim, S.H., Shi, Y., Hanson, K.A., Williams, L.M., Sakasai, R., Bowler, M.J., and Tibbetts, R.S. (2009). Potentiation of amyotrophic lateral sclerosis (ALS)-associated TDP-43 aggregation by the proteasome-targeting factor, ubiquilin 1. J. Biol. Chem. *284*, 8083–8092.

Koken, M.H., Puvion-Dutilleul, F., Guillemin, M.C., Viron, A., Linares-Cruz, G., Stuurman, N., de Jong, L., Szostecki, C., Calvo, F., Chomienne, C., et al. (1994). The t(15;17) translocation alters a nuclear body in a retinoic acid-reversible fashion. EMBO J. *13*, 1073–1083.

Kuo, P.H., Chiang, C.H., Wang, Y.T., Doudeva, L.G., and Yuan, H.S. (2014). The crystal structure of TDP-43 RRM1-DNA complex reveals the specific recognition for UG- and TG-rich nucleic acids. Nucleic Acids Res. *42*, 4712–4722.

Lee, E.B., Lee, V.M., and Trojanowski, J.Q. (2011). Gains or losses: molecular mechanisms of TDP43-mediated neurodegeneration. Nat. Rev. Neurosci. *13*, 38–50.

Li, Y.R., King, O.D., Shorter, J., and Gitler, A.D. (2013). Stress granules as crucibles of ALS pathogenesis. J. Cell Biol. *201*, 361–372.

Lin, Y., Protter, D.S., Rosen, M.K., and Parker, R. (2015). Formation and Maturation of Phase-Separated Liquid Droplets by RNA-Binding Proteins. Mol. Cell *60*, 208–219.

Liu-Yesucevitz, L., Bilgutay, A., Zhang, Y.J., Vanderweyde, T., Citro, A., Mehta, T., Zaarur, N., McKee, A., Bowser, R., Sherman, M., et al. (2010). Tar DNA binding protein-43 (TDP-43) associates with stress granules: analysis of cultured cells and pathological brain tissue. PLoS ONE *5*, e13250.

López-Otín, C., Blasco, M.A., Partridge, L., Serrano, M., and Kroemer, G. (2013). The hallmarks of aging. Cell *153*, 1194–1217.

Lukavsky, P.J., Daujotyte, D., Tollervey, J.R., Ule, J., Stuani, C., Buratti, E., Baralle, F.E., Damberger, F.F., and Allain, F.H. (2013). Molecular basis of UG-rich RNA recognition by the human splicing factor TDP-43. Nat. Struct. Mol. Biol. *20*, 1443–1449.

Maharana, S., Wang, J., Papadopoulos, D.K., Richter, D., Pozniakovsky, A., Poser, I., Bickle, M., Rizk, S., Guillén-Boixet, J., Franzmann, T.M., et al. (2018). RNA buffers the phase separation behavior of prion-like RNA binding proteins. Science *360*, 918–921.

Mann, J.R., Gleixner, A.M., Mauna, J.C., Gomes, E., DeChellis-Marks, M.R., Needham, P.G., Copley, K.E., Hurtle, B., Portz, B., Pyles, N.J., et al. (2019). RNA Binding Antagonizes Neurotoxic Phase Transitions of TDP-43. Neuron *102*, 321–338.e8.

Mariani, E., Frabetti, F., Tarozzi, A., Pelleri, M.C., Pizzetti, F., and Casadei, R. (2016). Meta-Analysis of Parkinson's Disease Transcriptome Data Using TRAM Software: Whole Substantia Nigra Tissue and Single Dopamine Neuron Differential Gene Expression. PLoS ONE *11*, e0161567.

McGurk, L., Gomes, E., Guo, L., Mojsilovic-Petrovic, J., Tran, V., Kalb, R.G., Shorter, J., and Bonini, N.M. (2018). Poly(ADP-Ribose) Prevents Pathological Phase Separation of TDP-43 by Promoting Liquid Demixing and Stress Granule Localization. Mol. Cell *71*, 703–717.e9.

Miguel, L., Frébourg, T., Campion, D., and Lecourtois, M. (2011). Both cytoplasmic and nuclear accumulations of the protein are neurotoxic in Drosophila models of TDP-43 proteinopathies. Neurobiol. Dis. *41*, 398–406.

Mito, M., Kawaguchi, T., Hirose, T., and Nakagawa, S. (2016). Simultaneous multicolor detection of RNA and proteins using super-resolution microscopy. Methods *98*, 158–165.

Modic, M., Grosch, M., Rot, G., Schirge, S., Lepko, T., Yamazaki, T., Lee, F.C.Y., Rusha, E., Shaposhnikov, D., Palo, M., et al. (2019). Cross-Regulation between TDP-43 and Paraspeckles Promotes Pluripotency-Differentiation Transition. Mol. Cell *74*, 951–965.e13.

Molliex, A., Temirov, J., Lee, J., Coughlin, M., Kanagaraj, A.P., Kim, H.J., Mittag, T., and Taylor, J.P. (2015). Phase separation by low complexity domains promotes stress granule assembly and drives pathological fibrillization. Cell *163*, 123–133.

Murray, D.T., Kato, M., Lin, Y., Thurber, K.R., Hung, I., McKnight, S.L., and Tycko, R. (2017). Structure of FUS Protein Fibrils and Its Relevance to Self-Assembly and Phase Separation of Low-Complexity Domains. Cell *171*, 615–627.e16.

Nakagawa, S., Yamazaki, T., and Hirose, T. (2018). Molecular dissection of nuclear paraspeckles: towards understanding the emerging world of the RNP milieu. Open Biol. *8*, 180150.

Namkoong, S., Ho, A., Woo, Y.M., Kwak, H., and Lee, J.H. (2018). Systematic Characterization of Stress-Induced RNA Granulation. Mol. Cell *70*, 175–187.e8.

Neumann, M., Sampathu, D.M., Kwong, L.K., Truax, A.C., Micsenyi, M.C., Chou, T.T., Bruce, J., Schuck, T., Grossman, M., Clark, C.M., et al. (2006).

Ubiquitinated TDP-43 in frontotemporal lobar degeneration and amyotrophic lateral sclerosis. Science *314*, 130–133.

Neumann, M., Kwong, L.K., Lee, E.B., Kremmer, E., Flatley, A., Xu, Y., Forman, M.S., Troost, D., Kretzschmar, H.A., Trojanowski, J.Q., and Lee, V.M. (2009). Phosphorylation of S409/410 of TDP-43 is a consistent feature in all sporadic and familial forms of TDP-43 proteinopathies. Acta Neuropathol. *117*, 137–149.

Nishimoto, Y., Nakagawa, S., Hirose, T., Okano, H.J., Takao, M., Shibata, S., Suyama, S., Kuwako, K., Imai, T., Murayama, S., et al. (2013). The long non-coding RNA nuclear-enriched abundant transcript 1_2 induces paraspeckle formation in the motor neuron during the early phase of amyotrophic lateral sclerosis. Mol. Brain *6*, 31.

Pinarbasi, E.S., Cağatay, T., Fung, H.Y.J., Li, Y.C., Chook, Y.M., and Thomas, P.J. (2018). Active nuclear import and passive nuclear export are the primary determinants of TDP-43 localization. Sci. Rep. *8*, 7083.

Polymenidou, M., Lagier-Tourenne, C., Hutt, K.R., Huelga, S.C., Moran, J., Liang, T.Y., Ling, S.C., Sun, E., Wancewicz, E., Mazur, C., et al. (2011). Long pre-mRNA depletion and RNA missplicing contribute to neuronal vulnerability from loss of TDP-43. Nat. Neurosci. *14*, 459–468.

Prasanth, K.V., Prasanth, S.G., Xuan, Z., Hearn, S., Freier, S.M., Bennett, C.F., Zhang, M.Q., and Spector, D.L. (2005). Regulating gene expression through RNA nuclear retention. Cell *123*, 249–263.

Puthiyedth, N., Riveros, C., Berretta, R., and Moscato, P. (2016). Identification of Differentially Expressed Genes Through Integrated Study of Alzheimer's Disease Affected Brain Regions. PLoS One *11*, e0152342.

Ramaswami, M., Taylor, J.P., and Parker, R. (2013). Altered ribostasis: RNA-protein granules in degenerative disorders. Cell *154*, 727–736.

Santama, N., Ogg, S.C., Malekkou, A., Zographos, S.E., Weis, K., and Lamond, A.I. (2005). Characterization of hCINAP, a novel coilin-interacting protein encoded by a transcript from the transcription factor TAFIID32 locus. J. Biol. Chem. *280*, 36429–36441.

Schirmer, L., Velmeshev, D., Holmqvist, S., Kaufmann, M., Werneburg, S., Jung, D., Vistnes, S., Stockley, J.H., Young, A., Steindel, M., et al. (2019). Neuronal vulnerability and multilineage diversity in multiple sclerosis. Nature *573*, 75–82.

Schmidt, H.B., and Rohatgi, R. (2016). In Vivo Formation of Vacuolated Multi-phase Compartments Lacking Membranes. Cell Rep. *16*, 1228–1236.

Shevtsov, S.P., and Dundr, M. (2011). Nucleation of nuclear bodies by RNA. Nat. Cell Biol. *13*, 167–173.

Stanėk, D., and Fox, A.H. (2017). Nuclear bodies: news insights into structure and function. Curr. Opin. Cell Biol. *46*, 94–101.

Sun, X., Duan, Y., Qin, C., Li, J.C., Duan, G., Deng, X., Ni, J., Cao, X., Xiang, K., Tian, K., et al. (2018). Distinct multilevel misregulations of Parkin and PINK1 revealed in cell and animal models of TDP-43 proteinopathy. Cell Death Dis. *9*, 953.

Taylor, J.P., Brown, R.H., Jr., and Cleveland, D.W. (2016). Decoding ALS: from genes to mechanism. Nature *539*, 197–206.

Udan-Johns, M., Bengoechea, R., Bell, S., Shao, J., Diamond, M.I., True, H.L., Weihl, C.C., and Baloh, R.H. (2014). Prion-like nuclear aggregation of TDP-43 during heat shock is regulated by HSP40/70 chaperones. Hum. Mol. Genet. *23*, 157–170.

Uversky, V.N. (2017). Intrinsically disordered proteins in overcrowded milieu: Membrane-less organelles, phase separation, and intrinsic disorder. Curr. Opin. Struct. Biol. *44*, 18–30.

van Es, M.A., Hardiman, O., Chio, A., Al-Chalabi, A., Pasterkamp, R.J., Veldink, J.H., and van den Berg, L.H. (2017). Amyotrophic lateral sclerosis. Lancet *390*, 2084–2098.

West, J.A., Mito, M., Kurosaka, S., Takumi, T., Tanegashima, C., Chujo, T., Yanaka, K., Kingston, R.E., Hirose, T., Bond, C., et al. (2016). Structural, super-resolution microscopy analysis of paraspeckle nuclear body organization. J. Cell Biol. *214*, 817–830.

Winton, M.J., Igaz, L.M., Wong, M.M., Kwong, L.K., Trojanowski, J.Q., and Lee, V.M. (2008). Disturbance of nuclear and cytoplasmic TAR DNA-binding protein (TDP-43) induces disease-like redistribution, sequestration, and aggregate formation. J. Biol. Chem. *283*, 13302–13309.

Xiang, S., Kato, M., Wu, L.C., Lin, Y., Ding, M., Zhang, Y., Yu, Y., and McKnight, S.L. (2015). The LC Domain of hnRNPA2 Adopts Similar Conformations in Hydrogel Polymers, Liquid-like Droplets, and Nuclei. Cell *163*, 829–839.

Yamazaki, T., Souquere, S., Chujo, T., Kobelke, S., Chong, Y.S., Fox, A.H., Bond, C.S., Nakagawa, S., Pierron, G., and Hirose, T. (2018). Functional Domains of NEAT1 Architectural lncRNA Induce Paraspeckle Assembly through Phase Separation. Mol. Cell *70*, 1038–1053.e7.

Zhao, M., Kim, J.R., van Bruggen, R., and Park, J. (2018). RNA-Binding Proteins in Amyotrophic Lateral Sclerosis. Mol. Cells *41*, 818–829.

STAR★METHODS

KEY RESOURCES TABLE

REAGENT or RESOURCE	SOURCE	IDENTIFIER
Antibodies		
Mouse anti-G3BP	BD Biosciences	Cat#611127; RRID:AB_398438
Rabbit anti-HA	Cell Signaling Technology	Cat#3724; RRID:AB_1549585
Rabbit anti-TIAR	Cell Signaling Technology	Cat#8509S; RRID:AB_10839263
Rabbit anti-SC35	Abcam	Cat#ab204916
Rabbit anti-SFPQ	Abcam	Cat#ab177149
Rabbit anti-TAF9	Abcam	Cat#ab169784
Rabbit anti-PML	Abcam	Cat#ab179466
Chicken anti-MAP2	Abcam	Cat#ab5392; RRID:AB_2138153
Mouse-anti-β-Tubulin III	Sigma-Aldrich	Cat#T2200; RRID:AB_262133
Mouse anti-FLAG	Sigma-Aldrich	Cat#F3165; RRID:AB_259529
Rabbit anti-c-Myc	Sigma-Aldrich	Cat#C3956; RRID:AB_439680
Mouse anti-HA	Proteintech	Cat#66006-1
Mouse anti-pS409/410-TDP-43	Proteintech	Cat#66318-1-Ig
Rabbit anti-TDP-43	Proteintech	Cat#10782-2-AP; RRID:AB_615042
Mouse anti-p54/nrb NONO	Santa Cruz	Cat#sc-166702; RRID:AB_2152178
Bacterial and Virus Strains		
BL21 (DE3) *E. coli*	TransGenBiotech	Cat#CD601-03
Chemicals, Peptides, and Recombinant Proteins		
TDP-43$^{1–274}$-K145/192Q	This study	N/A
TDP-43$^{1–274}$-K145/192R	This study	N/A
TDP-43$^{1–274}$-NES^{mut}	This study	N/A
TDP-43$^{1-274}$-NES^{mut}-K145/192R	This study	N/A
TDP-43$^{1–274}$-D169G	This study	N/A
Sumo-TDP-43	This study	N/A
Sumo-TDP-43-$^{1–274}$	This study	N/A
Sumo-TDP-43-ΔRRM1	This study	N/A
Sumo-TDP-43-ΔRRM2	This study	N/A
TDP-43$^{1–274}$	This study	N/A
TDP-43$^{1–274}$-ΔRRM1	This study	N/A
TDP-43$^{1–274}$-ΔRRM2	This study	N/A
Critical Commercial Assays		
Cell Counting Kit-8	Dojindo	Cat#CK04
CellTiter-Glo® Luminescent Assay	Promega	Cat#G7570
Experimental Models: Cell Lines		
293T	ATCC	ATCC® CRL-3216, RRID:CVCL_0063
HeLa	ATCC	ATCC® CCL-2, RRID:CVCL_0030
Primary cortical neurons	This study	N/A
Experimental Models: Organisms/Strains		
Drosophila: pBID-UASC-TDP-43-NES^{mut}	This study	N/A
Drosophila: pBID-UASC-TDP-43-D169G	This study	N/A
Drosophila: *D42*-Gal4	Bloomington *Drosophila* Stock Center	Strain#8816; RRID:BDSC_8816
Drosophila: *elav*-Gal4	Bloomington *Drosophila* Stock Center	Strain#8760; RRID:BDSC_8760

(*Continued on next page*)

Continued

REAGENT or RESOURCE	SOURCE	IDENTIFIER
Drosophila: UAS-*LacZ*	Bloomington *Drosophila* Stock Center	Strain#8529; RRID:BDSC_8529
Drosophila: pBID-UASC-Luciferase	Cao et al., 2017	N/A
Drosophila: pBID-UASC-TDP-43-WT	This study	N/A
Drosophila: pBID-UASC-TDP-43-NLS^{mut}	This study	N/A
Oligonucleotides		
PCR primer	This study	See Table S1
si*Ctrl*	Genepharma	5′–UUCUCCGAACGUGU CACGUTT –3′
si*NEAT1*	Genepharma	5′–UUACAAAAUAUGUUG CCAUTT –3′
Recombinant DNA		
pcDNA3.1-TDP-43-NES^{mut}-HA	This study	N/A
pcDNA3.1-TDP-43-K145/192Q-HA	This study	N/A
pcDNA3.1-TDP-43-HA	Sun et al., 2018	N/A
pcDNA3.1-TDP-43-NES^{mut}-K145/192R-HA	This study	N/A
pcDNA3.1-TDP-43-D169G-HA	This study	N/A
pcDNA3.1-TDP-43-Q331K-HA	This study	N/A
pcDNA3.1-TDP-43-M337V-HA	This study	N/A
pcDNA3.1-TDP43-ΔRRM1-HA	This study	N/A
pcDNA3.1-TDP43-ΔRRM2-HA	This study	N/A
pcDNA3.1-NEAT1	This study	N/A
pCMV-Myc-TDP-43$^{1–274}$	This study	N/A
pCMV-Myc-TDP-43-ΔRRM1	This study	N/A
pCMV-Myc-TDP-43-ΔRRM2	This study	N/A
pCAG-GFP-TDP-43	This study	N/A
pCAG-GFP-TDP-43-NES^{mut}	This study	N/A
pCAG-GFP-SFPQ	This study	N/A
pET28a-6 × His-TDP-43$^{1–274}$	This study	N/A
pET28a-6 × His-TDP-43$^{1–274}$-ΔRRM1	This study	N/A
pET28a-6 × His-TDP-43$^{1–274}$-ΔRRM2	This study	N/A
pET28a-6 × His-TDP-43$^{1–274}$-K145/192Q	This study	N/A
pET28a-6 × His-TDP-43$^{1–274}$-K145/192R	This study	N/A
pET28a-6 × His-TDP-43$^{1–274}$-NES^{mut}	This study	N/A
pET28a-6 × His-TDP-43$^{1-274}$-NES^{mut}-K145/192R	This study	N/A
pET28a-6 × His-TDP-43$^{1–274}$-D169G	This study	N/A
pET28a-6 × His-sumo-TDP-43	This study	N/A
pET28a-6 × His-sumo-TDP-43-$^{1–274}$	This study	N/A
pET28a-6 × His-sumo-ΔRRM1	This study	N/A
pET28a-6 × His-sumo-ΔRRM2	This study	N/A
pCMV-myc-TDP-43	Sun et al., 2018	N/A
pLenti-hSyn-TDP-43-HA	This study	N/A
pLenti-hSyn-TDP-43-ΔRRM1-HA	This study	N/A
pLenti-hSyn-TDP-43-ΔRRM2-HA	This study	N/A
pBID-UASC-TDP-43-Myc	This study	N/A
pBID-UASC-TDP-43-NLS^{mut}-Myc	This study	N/A
pBID-UASC-TDP-43-NES^{mut}-Myc	This study	N/A
pCAG-hTDP-43	Sun et al., 2018	N/A

(*Continued on next page*)

Continued

REAGENT or RESOURCE	SOURCE	IDENTIFIER
pcDNA3.1-TDP-43-NLS^{mut}-HA	This study	N/A
Software and Algorithms		
ImageJ	NIH	https://imagej.nih.gov/ij/
GraphPad Prism Software	GraphPad	https://www.graphpad.com/scientificsoftware/prism/
Leica Application Suite (LAS) X	Leica	https://www.leica-microsystems.com/products/microscope-software/p/leica-las-x-ls/

RESOURCE AVAILABILITY

Lead Contact

Further information and requests for resources and reagents should be directed to and will be fulfilled by the Lead Contact, Yanshan Fang (fangys@sioc.ac.cn).

Materials Availability

All unique and stable reagents generated in this study are available from the Lead Contact with a completed Material Transfer Agreement.

Data and Code Availability

This study did not generate datasets or code.

EXPERIMENTAL MODEL AND SUBJECT DETAILS

Drosophila strains and husbandry

The transgenic fly strains of WT and various mutant UAS-*hTDP-43* were generated by ΦC31 integrase-mediated, site-specific integration, which allowed uniform transgene expression across different lines. The attP2 landing site stock used for the fly embryo injection and transformation in this study was y[1] M{vas-int.Dm}ZH-2A w[*]; P{CaryP}attP40 (25C6). The pBID-UASC-Luciferase (UAS-Luc) transgenic fly strain was generated using the same approach at the same landing site (Cao et al., 2017) and was therefore used as a control in this study. The following strains were obtained from the Bloomington *Drosophila* Stock Center (BDSC): *D42*-Gal4 (#8816), *elav*-Gal4 (#8760) and UAS-*LacZ* (#8529). Flies were raised on standard cornmeal media and maintained at 25°C and 60% relative humidity. Flies tested in this study were all male flies. For western blot and immunostaining experiments, 5-day old adult flies were used. For aging-related experiments, the ages of the flies tested in each experiment are as indicated in the figures.

Mouse care and primary neuron culture

All mouse procedures were performed in compliance with the institutional guidelines on the scientific use of living animals at Interdisciplinary Research Center on Biology and Chemistry, the Chinese Academy of Sciences (CAS). Principles of laboratory animal care (NIH publication No. 86-23, revised 1985) were followed. Animal distress and conditions requiring euthanasia were addressed and the number of animals used was minimized.

Primary cortical neurons were isolated from the C57BL/6 mouse cortex at embryonic day 17 (E17, at which the gender of the embryos was not distinguishable) and cultured in serum-free Neurobasal medium (Invitrogen) supplemented with 2% B27, GlutaMax, and penicillin-streptomycin (Invitrogen). At 7 days *in vitro* (DIV), neurons were infected with pLenti-hSyn-TDP-43-HA for 5 days before extraction for RNA or immunofluorescence.

METHOD DETAILS

Plasmids and constructs

The pcDNA3.1-TDP-43-HA and pCMV-myc-TDP-43 plasmids were as previously described (Sun et al., 2018) and used as the templates to generate the following plasmids. The pcDNA3.1-TDP-43-NES^{mut}, NLS^{mut}, D169G, Q331K and M337V-HA plasmids were generated by site-directed mutagenesis using the Fast Mutagenesis Kit II (Vazyme). The pcDNA3.1-TDP-43-K145/192Q-HA and pcDNA3.1-TDP-43-NES^{mut}-K145/192R-HA plasmids were generated by site-directed mutagenesis using the Fast Mutagenesis Kit MultiS (Vazyme). The pCMV-myc-TDP-43$^{1-274}$ pCMV-myc-TDP-43-ΔRRM1, and pCMV-myc-TDP-43-ΔRRM2 plasmids were generated by PCR using the pCMV-myc-TDP-43 plasmid as a template. The pcDNA3.1-TDP43-ΔRRM1-HA and

pcDNA3.1-TDP43-ΔRRM2-HA plasmids were generated by PCR using the pCMV-myc-TDP-43-ΔRRM1 and pCMV-myc-TDP-43-ΔRRM2 plasmids as a template. To generate the pCAG-GFP-TDP-43 plasmid, the GFP coding sequence was amplified from pcDNA3.1-GFP-AXR3 (a gift from Dr. Z. Zhang) by PCR and then subcloned into a pCAG-hTDP-43 plasmid (Sun et al., 2018) using the ClonExpress MultiS One Step Cloning Kit (Vazyme). The pCAG-GFP-TDP-43-NES^{mut} plasmid was generated by site-directed mutagenesis using the Fast Mutagenesis Kit II (Vazyme). To generate the pCAG-GFP-SFPQ plasmid, The SFPQ coding sequence was amplified from pmEmerald-C1-SFPQ (a gift from Dr. L. Chen) by PCR and then subcloned into the pCAG-GFP-TDP-43 plasmid using the ClonExpress MultiS One Step Cloning Kit (Vazyme).

For generation of transgenic fly lines, WT and various mutant UAS-hTDP-43 constructs were generated by PCR using the above plasmids as a template and sub-cloned into the pBID-UASC-6*Myc vector (Cao et al., 2017) between the KpnI and ApaI sites.

For lentivirus infection of mouse primary neurons, the pLenti-hSyn-TDP-43-HA, pLenti-hSyn-TDP-43-ΔRRM1-HA and pLenti-hSyn-TDP-43-ΔRRM2-HA plasmid was generated by PCR using the pcDNA3.1-TDP-43-HA as a template and sub-cloned into the pLenti-hSyn vector (a gift from Dr. Y. Chen).

For *Escherichia coli* (*E. coli*) expression, the pET28a-6 × His-sumo-TDP-43, His-sumo-TDP-43-$^{1-274}$, His-sumo-TDP-43-ΔRRM1, His-sumo-TDP-43-ΔRRM2, His-TDP-43$^{1-274}$, His-TDP-43$^{1-274}$-ΔRRM1, His-TDP-43$^{1-274}$-ΔRRM2, His-TDP-43$^{1-274}$-K145/192Q, His-TDP-43$^{1-274}$-NES^{mut} and His-TDP-43$^{1-274}$-NES^{mut}-K145/192R and His-TDP-43$^{1-274}$-D169G constructs were generated by PCR using the above WT or mutant TDP-43 plasmid as a template and were sub-cloned into a pET28a-6 × His (a gift from Dr. L. Pan) or pET28a-6 × His-sumo (a gift from Dr. J. Zhou) vector. The His-TDP-43$^{1-274}$-K145/192R plasmid was generated by site-directed mutagenesis using the Fast Mutagenesis Kit MultiS (Vazyme) using the pET28a-6 × His-TDP-43$^{1-274}$ plasmid a template.

For *in vitro* transcription of NEAT1 RNA, the pcDNA3.1-NEAT1 was generated by PCR using the pEGFP-C1-mNEAT1 plasmid (a gift from Dr. L. Chen) as a template and sub-cloned into the pcDNA3.1 vector.

All constructs were verified by sequencing to ensure the integrity of the cloned open reading frames. The primers used for PCR to generate the expression plasmids are summarized in Table S1.

Lentivirus production

To generate lentivirus for infecting primary neurons, 293T cells were co-transfected with pLenti-hSyn-TDP-43-HA, psPAX2 and pMD2.G with a ratio of 4:2:1 in Opti-MEM medium using Lipofectamine 2000. Culture supernatant was collected at 48 h after transfection and passed through a 0.45-μm filter. Viral particles were concentrated from culture supernatants by Lenti-X Concentrator (Clontech). Viral pellets used for neuronal infection were resuspended in Neurobasal medium (Invitrogen).

Cell cultures and transfection

293T and HeLa cells were cultured in Dulbecco's Modified Eagle Medium (Sigma, D0819) supplemented with 10% (v/v) fetal bovine serum (FBS, BioWest) and 1% penicillin/streptomycin at 37°C in 5% CO_2. Transient transfection was performed using Lipofectamine 3000 (Invitrogen) in Opti-MEM (Invitrogen). Cells were transfected for at least 24 h before the subsequent drug treatments or examinations. For the KD experiment, the siRNA (Genepharma) was transfected into the HeLa cells using the Lipofectamine^{TM} RNAiMax Transfection Reagent (Invitrogen) according to the manufacturer's instruction. The siRNA was incubated for ~48 h before cells were harvested.

Pharmacological assays

Arsenite treatment: HeLa or 293T cells were grown on coverslips in a 24-well plate and transfected with the indicated plasmids for 24 h. Cells were then treated with 250 μM of $NaAsO_2$ or PBS for 30 min, prior to fixation with 4% paraformaldehyde. For the recovery experiments, the culture medium containing $NaAsO_2$ was removed and the cells were incubated in fresh medium for indicated time prior to fixation.

LMB treatment: For the nuclear export inhibition assays, LMB was added into the culture medium after 6 h transfection at indicated final concentrations.

CHX treatment: For the pulse-chase assays, CHX was added into the medium at a final concentration of 25 ng/mL.

MG132 treatment: For the proteasomal inhibition assays, MG132 was added into the medium at a final concentration of 25 μM.

CQ treatment: For autophagy inhibition assays, CQ was added into the medium a final concentration of 25 mM.

Cells incubated in the culture medium with the above drugs for indicated time before fixation for immunocytochemistry or western blotting analysis.

Immunocytochemistry and immunohistochemistry

HeLa or 293T cells grown on coverslips pre-coated with PLL (Sigma) in a 24-well plate were transfected and treated as described above. For immunostaining of whole-mount fly brains, the fly heads were dissected at the indicated ages in PBS on ice. The cells or fly brains were then fixed in 4% paraformaldehyde in PBS for 15 min at room temperature (RT), permeabilized in 0.5% Triton X-100 (Sigma) in PBS for 15~30 min and blocked with 3% goat serum in PBST (0.1% Triton X-100 in PBS) for 1 h at RT. The above primary and secondary antibodies were then incubated in the blocking buffer at 4°C overnight or for 48 h, or at RT for 1-2 h. After 3 washes with PBST, cells were mounted on glass slides using the VECTASHIELD Antifade Mounting Medium with DAPI (Vector Laboratories).

Confocal and super-resolution imaging

Fluorescent confocal images were taken with Leica TCS SP8 confocal microscopy system using a 63X or 100X oil objective (NA = 1.4). Super-resolution images were captured using the Leica SP8 LIGHTNING confocal microscope, which allowed simultaneous multicolor imaging in super-resolution down to 120 nm. Confocal or super-resolution images were then processed in LAS X (Leica) and assembled into figures using Adobe Photoshop CS6.

Live cell imaging

HeLa cells transfected with pCAG-GFP-TDP-43 were grown on Nunc Lab-Tek Chambered Coverglass (Thermo) for 24 h before the cells were treated with 250 μM of $NaAsO_2$. For live cell imaging, the chambered coverglasses were placed in the Incubation System for Microscopes (Tokai Hit) and maintained at 37°C in 5% CO_2 for the duration of the experiment. Time-lapse images were captured using the Leica TCS SP8 confocal microscopy system every 10 min for about 1 h.

FRAP assay

The Fluorescence recovery after photobleaching (PFRP) assay was performed using the FRAP module of the Leica SP8 confocal microscopy system. In brief, each GFP-TDP-43 NB was bleached using a 488 nm laser at 100% laser power for approximately 5 s. After photobleaching, time-lapse images were captured every 10 s for the about 5 min. For each indicated time point (t), the fluorescence intensity within the bleached NB was normalized to the fluorescence intensity of a nearby, unbleached NB (to control for photobleaching during prolonged live imaging). The normalized fluorescence intensity of pre-bleaching was set to 100% and the normalized fluorescence intensity at each time point (I_t) was used to calculate the fluorescence recovery according to the following formula: $FR(t) = I_t/I_{pre\text{-}bleaching}$. ImageJ was used for quantification and GraphPad Prism to plot and analyze the FRAP experiments.

Antibodies

The following antibodies were used for western blotting, immunoprecipitation and immunofluorescence assays: mouse anti-FLAG (Sigma, F3165), mouse anti-HA (Proteintech, 66006-1), mouse anti-pS409/410-TDP-43 (Proteintech, 66318-1-Ig), mouse anti-p54/nrb NONO (Santa Cruz, sc-166702), mouse anti-G3BP (BD Biosciences, 611127), rabbit anti-HA (CST, C29F4), rabbit anti-c-Myc (Sigma, c3956), rabbit anti-TDP-43 (Proteintech, 10782-2-AP), anti-β-Tubulin III (Sigma, T2200), rabbit anti-TIAR (Cell Signaling Technology, 8509S), rabbit anti-SC35 (Abcam, ab204916), rabbit anti-SFPQ (Abcam, ab177149), rabbit anti-TAF9 (Abcam, ab169784), rabbit anti-PML (Abcam, ab179466), and chicken anti-MAP2 (Abcam, ab5392). HRP conjugated secondary antibodies: goat anti-mouse (Sigma, A4416) and goat anti-rabbit (Sigma, A9169). Fluorescent secondary antibodies: goat anti-mouse-Alexa Fluor 488 (Life Technologies, A11029), goat anti-rabbit-Alexa Fluor 568 (Life Technologies, A11036) and goat anti-Chicken-Alexa Fluor 568 (Life Technologies, A11041).

Protein extraction and western blotting

Total protein was extracted from cells in a 2% SDS extraction buffer (50 mM Tris pH 6.8, 2% SDS, 1% mercaptoethanol, 12.5% glycerol and 0.04% bromophenol blue) containing the protease inhibitor cocktail (Roche, 04693132001). For separation of soluble and insoluble proteins, cells or fly heads were lysed on ice in a RIPA buffer (50 mM Tris pH 8.0, 150 mM NaCl, 1% NP-40, 5 mM EDTA, 0.5% sodium deoxycholate, 0.1% SDS) supplemented with protease and phosphatase inhibitors (Roche). After sonication, the homogenates were centrifuged at 16,000 g for 15min at 4°C. The supernatant was used as the soluble fraction and the pellets containing the insoluble fraction were dissolved in a urea buffer (9 M urea, 50 mM Tris buffer, pH 8.0) after wash.

All protein samples were then boiled at 100°C for 5 min and separated using a 10% Bis-Tris SDS-PAGE (Invitrogen). Detection was performed using the High-sig ECL Western Blotting Substrate (Tanon). Images were captured using an Amersham Imager 600 (GE Healthcare) and densitometry was measured using ImageQuant TL Software (GE Healthcare). The contrast and brightness were optimized equally using Adobe Photoshop CS6. All experiments were normalized to tubulin or GAPDH as indicated in the figures.

Cell viability assay

Transfected 293T cells were seeded in 96-well plates (Corning) at the density of 9×10^3 cells/well and cultured in 100 μL of culture medium. Otherwise, cell viability was examined 48-72 h after transfection using the Cell Counting Kit-8 (CCK-8) (Dojindo), according to the manufacturer's instructions. Briefly, 10 μL of the CCK-8 solution were added to each well and incubated at 37°C for 2.5 h. Finally, the absorbance at 450 nm was measured with a Synergy2 microplate reader (BioTek Instruments).

ATP level measurement

Transfected 293T cells were seeded in 96-well plates (Corning) at the density of 2.5×10^4 cells/well. ATP levels were examined 36 h after transfection using the CellTiter-Glo® Luminescent Assay (Promega) according to the manufacturer's instructions. Briefly, the CellTiter-Glo® reagent was added into the microplate wells, mixed and incubated for 15 min at 37°C on the shaker. The luminescence was then measured with a Synergy2 microplate reader (BioTek Instruments).

RNA extraction and real-time quantitative PCR

For quantitative PCR (qPCR), total RNA was isolated from mouse primary neuron using TRIzol (Invitrogen) according to the manufacturer's instruction. After DNase (Promega) treatment, the reverse transcription reactions were performed using All-in-One cDNA Synthesis SuperMix kit (Bimake). The cDNA was then used for real-time qPCR using the SYBR Green qPCR Master Mix (Bimake) with the QuantStudio 6 Flex Real-Time PCR system (Life Technologies). The mRNA levels of GAPDH were used as an internal control to normalize the mRNA levels of *NEAT1*. The qPCR primers used in this study are listed below:

Total *mNEAT1*:
5′- ACTCTTGCCCCTCACTCTGA −3′
5′- CAGGGTGTCCTCCACCTTTA −3′;
mNEAT1_2:
5′- CCCACACCTCAGTGGTTTCT −3′
5′- ACAGAACCAAGGCACAATCC −3′;
mGAPDH:
5′- CACCATCTTCCAGGAGCGAG −3′
5′- CCTTCTCCATGGTGGTGAAGAC −3′;

Purification of TDP-43 proteins

WT or mutant TDP-43 protein was expressed in BL21 (DE3) *E. coli* (TransGenBiotech, CD601-03) at 19°C for 16 h after induction by adding 100 μM of IPTG as previously described (*46*). In brief, cells were harvested by centrifugation at 4000 rpm for 20 min at 4°C and lysed in 50 mL of lysis buffer (50 mM Tris-HCl, 500 mM NaCl, pH 8.0, 10 mM imidazole, 4 mM β-mercaptoethanol, 1 mM PMSF, and 0.1 mg/mL RNase A). After cell lysates were filtered with a 0.22 μm filter, the protein was purified using Ni columns (GE Healthcare, USA) and then eluted in an elution buffer (50 mM Tris-HCl, 500 mM NaCl, pH 8.0, 250 mM imidazole and 4 mM β-mercaptoethanol). The proteins were further purified using the Superdex 200 16/600 columns (GE Healthcare) in a buffer containing 50 mM Tris-HCl pH 7.5, 300 mM NaCl and 2 mM DTT, and freshly frozen in liquid nitrogen and stored at −80°C. RNase A was routinely added in cell lysates and administrated again before chromatography during the protein purification procedure. All purified proteins were confirmed by Coomassie brilliant blue staining and western blotting before use.

Dot-blot RNA-protein binding assay

Purified WT or mutant TDP-43 protein was diluted in a blotting buffer (50 mM Tris-HCl, pH 7.5, 300 mM NaCl, and 5% glycerol) and blotted onto a 0.45 μm nitrocellulose membrane. The membranes were left to dry at room temperature for 30 min and then stained with Ponceau S for 10 s. Images were captured using an Amersham Imager 600 (GE Healthcare). After the images were captured using an Amersham Imager 600 (GE Healthcare), the membranes were washed with PBST (0.05% TWEEN 20 in PBS) for 30 min and then incubated in the PBST containing 25 ng/μl total RNAs or NEAT1 RNA for 1 h with gentle rocking and rotation at room temperature. The membranes were then washed in PBST and incubated in the SYBR Gold Nucleic Acid Gel Stain (Invitrogen) for 10 min. RNAs bound to the membranes were imaged and examined using the Gel Image System (Tanon).

In vitro phase separation and RNA buffering assay

For the *in vitro* LLPS experiments, purified WT or mutant TDP-43 protein was mixed with NaCl at indicated concentrations in a phase separation buffer (50 mM Tris-HCl, pH 7.5 and 5%–10% (w/v) PEG 8000 (Sigma)) and incubated for 1 min at room temperature. For the RNA buffering assay, the TDP-43 proteins were incubated with total RNAs, tRNA or NEAT1 RNA in the above phase separation buffer with NaCl at indicated concentrations as shown in the figures. Finally, 5 μL of each sample was pipetted onto a coverslip and imaged using a Leica microscope with differential interference contrast (DIC). The total RNAs were extracted from HeLa cells using TRIzol (Invitrogen) according to the manufacturer's instructions. Yeast tRNA was purchased from Invitrogen. The NEAT1 RNA was *in vitro* transcribed and purified using HiScribe T7 Quick High Yield RNA Synthesis Kit (NEB). Total RNAs and NEAT1 RNA were used within one day of production.

Electrophoretic mobility-shift assay

To examine the RNA binding affinity of WT and D169G TDP-43, the purified TDP-$43^{1\text{-}274}$ protein was incubated with *NETA1* RNA in a buffer containing 50 mM Tris-HCl, 500 mM NaCl, pH 8.0 at 37°C for 10 min, and then loaded in 0.65% UltraPure Agarose (Thermo) and examined by electrophoresis. The RNA was visualized using the SYBRTM Green II RNA Gel Stain (Invitrogen) in 0.5 X TBE buffer and imaged with UV light using the Gel Image System (Tanon).

Fluorescence *in situ* hybridization

The fluorescently-labeled DNA probes used in the Fluorescence *in situ* hybridization (FISH) assay to detect *NEAT1* lncRNA were synthesized with the Nick Translation DNA Labeling System (Enzo) and Gold 550 dUTP (Enzo). The *NEAT1_2* cDNA templates used in the

above reactions were generated from human HeLa cells or mouse NSC-34 cells by reverse transcription reactions (TaKaRa) using the following primers:

Human *NEAT1_2* mid1:
5′-GCCACATTCTTTGCCTTCAT-3′;
5′-TCATTTACCCGCATTTCACA-3′

The FISH assay was conducted as previously described (Mito et al., 2016). Briefly, cells grown on coverslips were fixed in 4% paraformaldehyde (PBS) for 30 min at room temperature (RT), washed twice with PBS, and permeabilized in 0.5% Triton X-100 (Sigma) and 2 mM rnase-inhibitor-ribonucleoside-vanadyl complexes (RVC) (Sangon Biotech) in PBS for 30 min at RT. The hybridization buffer containing the fluorescent labeled DNA probes (10 ng/μl) in 50% Formamide (Sangon Biotech), 2x saline sodium citrate (SSC) (Invitrogen) and 500 μg/mL Salmon Sperm DNA Solution (Invitrogen) was heated at 100°C for 10 min and placed on ice before incubated with the samples at 37°C overnight. For the simultaneous detection of TDP-43, immunocytochemistry was performed afterward as mentioned above.

Eye degeneration analysis and climbing assay in flies

To assess the eye degeneration, z stack images of adult fly eyes were captured using an Olympus SZX16 stereomicroscope at indicated ages. Degeneration was evident and assessed by rough surface, swelling and loss of pigment cells of the compound eyes. Each fly eye was single-blindly scored in a scale of 0 to 4, with 0 for no degeneration and 4 for the full degeneration.

For the climbing assay, ~20 flies per vial, 5~10 vials per group were tested. All flies were transferred into an empty polystyrene vial and allowed 15 min for flies to recover. The flies were then gently tapped down to the bottom of the vial and the number of flies that climbed over 3 cm within 10 s was recorded. The test was repeated three times for each vial and the average was used in the quantifications.

QUANTIFICATION AND STATISTICAL ANALYSIS

Statistical significance in this study is determined by one-way analysis of variance (ANOVA) with Tukey's HSD post hoc test, two-way ANOVA with Bonferroni's post hoc test, or unpaired, two-tailed Student's t test with unequal variance at $*p < 0.05$, $**p < 0.01$, and $***p < 0.001$ and specified in the legends of each figure. Error bars represent the standard error of the mean (SEM).